J. Fluid Mech. (2003), *vol.* 483, *pp.* 1–36.
DOI: 10.1017/S0022112003003859 Printed in the United Kingdom

Cycle-induced flow and transport in a model of alveolar liquid lining

By HSIEN-HUNG WEI[1], STEVEN W. BENINTENDI[2], DAVID HALPERN[3] AND JAMES B. GROTBERG[1]

[1]Department of Biomedical Engineering, University of Michigan, Ann Arbor, MI 48109, USA

[2]University of Dayton, Dayton, OH 45469-2760, USA

[3]Department of Mathematics, University of Alabama, Tuscaloosa, AL 35487, USA

(Received 1 May 2001 and in revised form 19 November 2002)

A simplified model is developed for an alveolar liquid lining undergoing cyclic stretching which mimics breathing motions. A thin, viscous film coats an extensible alveolar wall with small aspect ratio, ε. Scaling analysis and asymptotic theory are used to describe the interface profile and surfactant distribution during the oscillation cycle for either insoluble or soluble surfactants. The flow consists of two distinct regimes: an outer region away from the rigid endwalls where flow is near-parallel and a boundary-layer region at the rigid endwalls where flow is non-parallel. The system is solved asymptotically in the limit of $\varepsilon \ll 1$ and small strain amplitudes, $\Delta \ll 1$. For leading order in ε, steady streaming vortical flows are found at $O(\Delta^2)$ and their size, number and flow direction depend on the system parameter values. This preliminary model can be useful for understanding alveolar transport characteristics for slowly diffusing molecules with large Péclet number, such as endogenous surfactants and proteins as well as delivered surfactants, drugs and genetic material that may occur in various therapies or partial liquid ventilation. The flow pattern also provides a pathway for cell–cell signalling within the alveolus.

1. Introduction

The thin liquid layer coating the alveolar wall is an essential feature in alveolar homeostasis. It is the compartment between the alveolar cell surface and the air–liquid interface where surface tension dominates lung mechanical behaviour to a large extent. Surfactants and proteins produced and absorbed by alveolar type II cells traverse the liquid layer in either direction as part of their normal metabolism (Wright & Clements 1987; Lewis, Ikegami & Jobe 1992) that keeps interfacial surface tensions low and the normal lung, therefore, fairly compliant. Because of their size and complexity, the surfactants and proteins diffuse quite slowly compared to respiratory gases, which must also cross this liquid barrier. Thus, convective transport via flows across the liquid layer for large molecules is an important aspect of alveolar homeostasis. Also, flow parallel to the cellular boundaries provides a potential route for cell–cell signalling since bioactive molecules produced by an alveolar cell can influence its neighbours. Hence, some understanding of possible flow patterns in the alveolar liquid lining can lead to a better appreciation of overall pulmonary behaviour.

In addition to normal or abnormal homeostasis, there are several clinical methodologies that involve delivery of large molecular species to the alveoli via the airways. Examples are surfactant replacement therapy (SRT) (Zelter *et al.* 1990; Corbet *et al.*

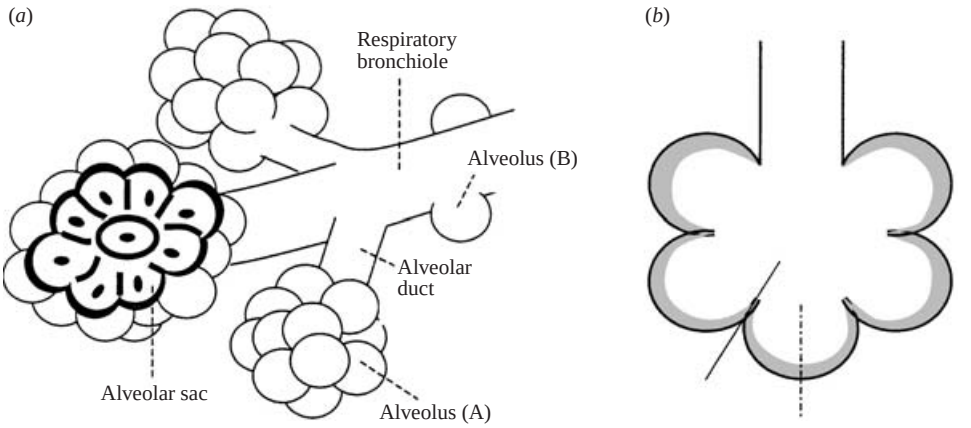

FIGURE 1. (*a*) Respiratory bronchiole and alveoli. We study the alveolus 'A' which is in a cluster of alveoli. The alveolus 'B' is directly attached to the airway, and is studied by Podgorski & Gradon (1993). (*b*) A cluster of several alveoli. The insolated alveolus is used to develop a simplified model problem.

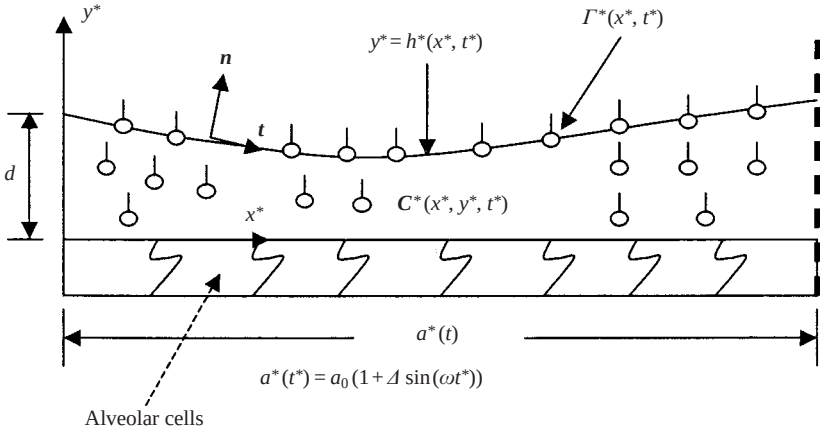

FIGURE 2. A stretchable two-dimensional liquid-filled slot in the presence of insoluble or soluble surfactants.

1991; Jobe 1993; Halpern, Jensen & Grotberg 1998), partial liquid ventilation (PLV) (Mates *et al.* 1994; Hirschl *et al.* 1995; Shaffer & Wolfson 1996; Tarczy-Hornoch *et al.* 1998) which may also include drug or gene delivery (Wolfson, Greenspan & Shaffer 1996; Fox *et al.* 1997; Lisby *et al.* 1997) and inhaled administration of various medications or genetic material (Meisner, Pringle & Mezei 1989; Davis *et al.* 1992; Flotte 1993; Edwards *et al.* 1997; Waldrep *et al.* 1997; Yu & Chien 1997; Raczka *et al.* 1998). In all of these examples, the role that alveolar liquid lining flow patterns may play in the delivery process is unknown.

The cluster of alveoli, or alveolar sac, highlighted in figure 1(*a*) and shown in figure 1(*b*), is a representative of the termination of the bronchial tree. A single alveolus is approximately 200 μm in diameter and is made up of both type I and II cells. Type I cells comprise about 90% of the alveolar surface while type II cells make up the remaining 10% (Crapo *et al.* 1982). Therefore, a typical alveolar membrane surface is made of many alveolar cells and the liquid film (shaded layer) covers them all as in figure 2. The liquid film, then, is a potential route of cell–cell communication and

the present model will address flows in the film that can provide such transport and signal pathways.

The purpose of our study is to examine a model of alveolar liquid flow resulting from breathing motions in concert with the influence of surface tension, both from capillarity and Marangoni effects. The flow of the liquid lining along airways often has similar flow mechanisms to the alveolar flow. It has been extensively studied, particularly for surfactant transport. When surfactant is instilled in the trachea, forced air and gravity dominate the flow in the upper airways while capillary and Marangoni flows dominate in the smaller airways. Marangoni spreading without including capillarity and breathing motions has been studied by Borgas & Grotberg (1988), Gaver & Grotberg (1990), Halpern & Grotberg (1992), Jensen & Grotberg (1992, 1993), Espinosa *et al.* (1993), Grotberg, Halpern & Jensen (1995) and Bull *et al.* (1999). These models employed lubrication theory for describing the evolution of the liquid layer and surfactant distribution.

Additional models including oscillatory wall strain can be found in Gradon & Podgorski (1989) and Podgorski & Gradon (1990, 1991). Although the Gradon & Podgorski (1989) and Podgorski & Gradon (1990) models simplified the alveolar geometry to be locally planar, the predictions behaved well in predicting the optimal alveolar size for liquid clearance. Their subsequent work (Podgorski & Gradon 1993) applied a spherical model and found similar qualitative features to their planar models. The model in Podgorski & Gradon (1993) predicts that fluid and surfactants are pumped out of the alveolus owing to Marangoni flows generated by wall oscillations. Such a result corresponds to an alveolus similar to that labelled 'B' in figure 1(*a*), one that is connected directly to an airway whose ability to take new fluid and surfactant is not limited by their assumptions. It is more difficult to envisage that model as pertaining to an alveolus similar to that labelled 'A' in figure 1(*a*) which is surrounded by other alveoli, since they would all be pumping liquid out with no neighbours predicted to accept the liquid. A more complex model would be required to handle flow from one alveolus to another.

Espinosa & Kamm (1997) modelled the liquid lining of an airway and its behaviour when a non-uniform, oscillatory axial wall strain is applied in the presence of a soluble surfactant. They modelled sorption kinetics assuming a constant bulk concentration of surfactant. The predictions are for net fluid transport toward the stiffer end of the airway, corresponding to the proximal end of the bronchial tree. They also mentioned that their model could be used to develop an understanding of liquid flows near an alveolar corner created by two septal planes. In all of the above analyses, however, capillarity is negligible owing to relatively low surface tension in an environment of normal surfactant levels. These studies suggest that the wall's periodic motion encourages clearance of liquid from the lung, though no process is modelled to replace the liquid for maintaining homeostasis. Zelig & Haber (2002) considered a fluid and surfactant replacement model allowing cross-flow through the alveolar wall to maintain average alveolar liquid volume.

In the present study, we are interested in alveolus 'A' of figure 1(*a*). This alveolus is surrounded by many other alveoli, and is not near an airway. We describe such alveoli as having a two-dimensional, cluster-type structure as depicted in figure 1(*b*). A thin liquid layer with a soluble surfactant coats the inside of the alveolus. During expiration, the alveolus contracts and the film thickens whereas for inspiration, the alveolus expands and the film thins. In this case, we assume there is no net transport between adjacent alveoli within the time scale of an oscillation. For simplicity, we shall follow Podgorski & Gradon (1990) with the assumption of impermeable alveolar

walls and choose a pinned-end condition such that the interface is fixed at the vicinity of alveolar outlet. However, we choose a no-flux condition for surfactant and liquid at the outlet in order to understand an 'A-type' alveolus better.

Let us discuss further the liquid lining in an alveolus. The thickness of the fluid layer is about 0.1 μm (Bastacky *et al.* 1995) and much smaller than an alveolar diameter. In fact, an alveolus can be regarded as consisting of flat septal faces. The liquid lining is continuous and is approximately flat along most of the alveolar wall, except near the septal intersections where the layer can be thicker. Espinosa & Kamm (1997) have proposed that flow in these corners owing to wall oscillations may be a means of preventing dry spots on the alveolar wall. However, our model deals with larger-scale motions based on the entire alveolar geometry. Since flat wall regions normally occupy most portions of the periphery of the alveolar membrane, we can regard the thin-layer region as the primary flow contribution.

In this paper, we model the alveolar flow as in figure 2, which describes a two-dimensional, liquid-filled system that undergoes a sinusoidal oscillation and contains insoluble or soluble surfactants at the interface. Note that in order to assess the impact of the capillary force particularly due to the alveolar wall's curvature, as we see later in the formulation, we add the corresponding term to the interfacial curvature in the normal stress condition. We shall apply lubrication theory to derive a set of coupled evolution equations for the liquid thickness and surfactant distribution in our model. However, lubrication theory is only valid for the flow region far away from the pinned wall. For completeness, the flow should consist of two distinct regions: the outer core region described by lubrication theory, and the inner rigid endwall region. Similar to Sen & Davis (1982) for thermocapillary flows, and Cormack, Leal & Imberger (1974) for natural convection flows, we also develop a matched asymptotic theory to solve the inner region problem in the present problem.

2. Mathematical model

2.1. *Governing equations and boundary conditions*

We consider a viscous fluid layer with density, ρ, and viscosity, μ lying on a planar stretchable membrane as shown in figure 2. The fluid is pinned at the left-hand end of the wall with height d. The membrane underneath the fluid extends or contracts in the x^*-direction during inhaling or exhaling of a breathing cycle. The length of the (half) membrane is $a^*(t)$ with its cycle-average length a_0. The right-hand end at $x^* = a^*(t)$ is a line of symmetry. The air–liquid interface is denoted by $y^* = h^*(x^*, t^*)$. The flow velocities in the x^* and y^* components are u^* and v^*, respectively, and the pressure is p^*. The liquid layer contains a soluble surfactant with the bulk concentration $C^*(x^*, y^*, t^*)$ and the surface concentration $\Gamma^*(x^*, t^*)$ at the interface.

The governing equations for fluid's motions are

$$\nabla^* \cdot \boldsymbol{v}^* = 0, \tag{2.1}$$

$$\rho[\boldsymbol{v}^*_{t^*} + \boldsymbol{v}^* \cdot \nabla^* \boldsymbol{v}^*] = -\nabla^* p^* + \mu \nabla^{*2} \boldsymbol{v}^* + \rho \boldsymbol{g}^*, \tag{2.2}$$

where $\boldsymbol{g}^*$ is the gravitational vector. The system is subject to the following boundary conditions for the flow problem.

Along the stretching impermeable membrane wall at $y^* = 0$, the fluid and wall velocities are equal,

$$u^*(x^*, 0, t^*) = u^*_{wall}(x^*, t^*),\ v^*(x^*, 0, t^*) = 0, \tag{2.3}$$

where u^*_{wall} is the velocity of the membrane. Owing to periodic breathing, the length $a^*(t^*)$ of the membrane varies with time in the following manner:

$$a^*(t) = a_0(1 + \Delta \sin(\omega t^*)), \tag{2.4}$$

where Δ is the strain amplitude of membrane stretching and ω is the breathing frequency. Then assuming a model of uniform strain, the location of a material point $\xi^* \in [0, a_0]$ is expressed as $x^* = \xi^*[1 + \Delta \sin(\omega t^*)]$. Then the wall velocity is

$$u^*_{wall} = \xi^* \omega \Delta \cos(\omega t^*) = \frac{\Delta \cos(\omega t^*)}{1 + \Delta \sin(\omega t^*)} x^*. \tag{2.5}$$

As a result, u^*_{wall} is proportional to x^* at any instant.

For the lateral boundaries, we impose a pinned condition and a symmetry condition for the interface shape:

$$h^*(0, t^*) = d/a_0, \tag{2.6}$$

$$h^*_x(a^*(t^*), t^*) = 0. \tag{2.7}$$

The no-slip and no-penetration conditions at the pinned wall are

$$u^*(0, y^*, t) = v^*(0, y^*, t) = 0. \tag{2.8}$$

There is more discussion about the boundary conditions at the pinned wall in § 5.5. Since the fluid volume is conserved in the domain, applying $h^*_{t^*} = -Q^*_{x^*}$ where $Q^*(x^*, t^*)$ is the local flow rate across the fluid layer, and Leibnitz formula for differentiating an integral yields

$$Q^*(a(t^*), t^*) = (u^*_{wall} h^*)|_{x=a^*(t^*)}. \tag{2.9}$$

As we shall see later, this condition will be used for boundary conditions of the liquid thickness and the surfactant concentration for the outer flow region in § 3.

At the interface $y^* = h^*(x^*, t^*)$, the kinematic condition is

$$h^*_{t^*} + u^* h^*_{x^*} - v^* = 0. \tag{2.10}$$

The normal and tangential stress balances on the interface are, respectively,

$$-p^* + \mu \boldsymbol{n} \cdot (\nabla^* \boldsymbol{v}^* + \nabla^* \boldsymbol{v}^{*T}) \cdot \boldsymbol{n} = -\sigma^* (\nabla^*_s \cdot \boldsymbol{n}), \tag{2.11}$$

$$\mu \boldsymbol{t} \cdot (\nabla^* \boldsymbol{v}^* + \nabla^* \boldsymbol{v}^{*T}) \cdot \boldsymbol{n} = \boldsymbol{t} \cdot \nabla^*_s \sigma^*, \tag{2.12}$$

where $\boldsymbol{n}$ and $\boldsymbol{t}$ are unit normal and tangential vectors of the interface as defined in figure 2, $\nabla^*_s = (\boldsymbol{I} - \boldsymbol{nn}) \cdot \nabla^*$ is the surface gradient operator, σ^* is the surface tension and is a function of the surface concentration Γ^*. For simplicity, we assume a linear equation of state for $\sigma^*(\Gamma^*)$:

$$\sigma^* = \sigma^*_0 - \left(\frac{\partial \sigma^*}{\partial \Gamma^*} \right)_0 (\Gamma^* - \Gamma^*_0), \tag{2.13}$$

where σ^*_0 and Γ^*_0 are the surface tension and the corresponding surface concentration for the non-stretching system. For a normal lung, Γ^* could be as high as the maximum packing density of surfactants Γ^*_∞. However, for a lung with respiratory disease due to lack of surfactants, the surfactant concentration could be very dilute ($\Gamma^* \ll \Gamma^*_\infty$). Since most previous studies for modelling alveolar flow are focused on high-concentration regimes as occurs in a normal lung, we would like to extend the analysis to the case where surfactants are lacking. We shall discuss this in more detail in the next subsection.

The normal stress condition contains capillary forces working together with the curvature of the interface $\nabla_s^* \cdot \boldsymbol{n}$. The surface tension gradient due to non-uniform surfactant distribution along the interface generates the Marangoni force, which creates a flow from a region of lower surface tension (higher surfactant concentration) to a region of higher surface tension (lower surfactant concentration). The Marangoni stress balances viscous shear in the tangential stress condition, (2.12).

The surfactant transport along the interface is described by the following equation (Stone 1990):

$$\Gamma_{t^*}^* + \nabla_s^* \cdot (\boldsymbol{v}_s^* \Gamma^*) - D_s \nabla_s^{*2} \Gamma^* + (\nabla_s^* \cdot \boldsymbol{n}) \Gamma^* (\boldsymbol{v}^* \cdot \boldsymbol{n}) = J^*, \tag{2.14}$$

where the surface diffusivity is D_s, $\boldsymbol{v}_s^*$ is the surface velocity, and $\boldsymbol{v}^* \cdot \boldsymbol{n}$ in the normal velocity component to the interface. For the left-hand side of (2.14), the first three terms represent the accumulation, the surface convection and surface diffusion, while the last term is the variation in surfactant concentration resulting from the local stretching and deformation of the interface. On the right-hand side of (2.14), J^* is a diffusive flux from the bulk to the interface. This flux is equal to the net sorption flux at the interface. We assume linear sorption kinetics in the form:

$$J^* = k_1 C_s^* - k_2 \Gamma^* = -D_b (\boldsymbol{n} \cdot \nabla C^*)|_{y^* = h^*}, \tag{2.15}$$

where k_1 and k_2 are the rate constants of adsorption and desorption, respectively, and C_s^* denotes the surface sublayer concentration. D_b is the bulk diffusivity.

The bulk concentration is governed by the convection–diffusion equation,

$$C_{t^*}^* + \boldsymbol{v}^* \cdot \nabla C^* = D_b \nabla^2 C^*. \tag{2.16}$$

We assume that surfactants are impermeable to the membrane for this first model. Therefore, the boundary condition is

$$C_{y^*}^*(x^*, 0, t^*) = 0. \tag{2.17}$$

Similarly, the impermeable and symmetry conditions at the lateral boundaries require

$$C_{x^*}^*(0, y^*, t^*) = C_{x^*}^*(a^*(t^*), y^*, t^*) = 0. \tag{2.18}$$

We also have two global constraints because neither fluid nor surfactants leave the domain. They are consequences of transport equations and boundary conditions. The volume of the liquid film has to be a constant:

$$\int_0^{a^*(t^*)} h^*(x^*, t^*)\, \mathrm{d}x^* = V_0^*, \tag{2.19}$$

where V_0^* is the volume (per unit length) of liquid. For the surfactant,

$$\int_0^{a^*(t^*)} \Gamma^*(x^*, t^*)\, \mathrm{d}s^* + \int_0^{a^*(t^*)} \int_0^{h^*(x^*, t^*)} C(x^*, y^*, t^*)\, \mathrm{d}y^*\, \mathrm{d}x^* = M_s^*, \tag{2.20}$$

where $\mathrm{d}s^*$ is a differential arclength along the interface, and M_s^* is the total amount of the surfactant.

2.2. *Scaling*

We now non-dimensionalize the problem according to the following scales:

$$\left.\begin{aligned} t = \omega t^*, \quad x = \frac{x^*}{a_0}, \quad y = \frac{y^*}{d}, \quad u = \frac{u^*}{U}, \quad v = \frac{v^*}{(Ud/a_0)}, \\ p = \frac{p^*}{(\mu a_0 U/d^2)}, \quad \sigma = \frac{\sigma^*}{\sigma_0^*}, \quad \hat{\Gamma} = \frac{\Gamma^*}{\Gamma_\infty^*}, \quad \hat{C} = \frac{C^*}{(k_2\Gamma_\infty^*/k_1)}, \end{aligned}\right\} \tag{2.21}$$

where $U = \omega a_0$ is a characteristic velocity. Since gravity is negligible at the alveolar level, the dimensionless governing equations for the fluid motions are

$$u_x + v_y = 0, \tag{2.22}$$

$$Re\,\varepsilon^2[u_t + uu_x + vu_y] = -p_x + \varepsilon^2 u_{xx} + u_{yy}, \tag{2.23a}$$

$$Re\,\varepsilon^4[v_t + uv_x + vv_y] = -p_y + \varepsilon^4 v_{xx} + \varepsilon^2 v_{yy}, \tag{2.23b}$$

where we introduce an aspect ratio $\varepsilon = d/a_0 \ll 1$ in the present problem, since the thickness of the fluid layer is about 0.1 μm (Bastacky *et al.* 1995). The Reynolds number and the capillary number are given by $Re = \rho\omega a_0^2/\mu$ and $Ca = \mu\omega a_0/\sigma_0^*$, respectively. An alveolus has an average 200 μm diameter (so that half periphery $a_0 = 157\,\mu\text{m}$). For a normal lung, the thickness of a coating fluid layer is about 0.1 μm. In PLV application, however, the fluid layer is expected to be thicker, but no definite data are available. The present analysis is still applicable to the situation even when the thickness during PLV is about ten times the normal because it is still thin compared to the size of the alveolus. Thus, ε ranges from $O(10^{-3})$ to $O(10^{-2})$. Assume that $\mu = 0.01\,\text{g cm}^{-1}\,\text{s}^{-1}$ and $\rho = 1.0$ g cm^{-3} for the fluid. Consider the normal breathing frequency of 12 times/min, corresponding to $\omega \approx 1$, then Re is $O(10^{-2})$. The surface tension $\sigma_0^* = 1$–$70\,\text{dyn cm}^{-1}$ yields $Ca = 10^{-4}$–10^{-6}.

The boundary conditions at the wall are

$$u(x, 0, t) = u_{wall}(x, t),\ v(x, 0, t) = 0, \tag{2.24}$$

where

$$u_{wall} = \frac{\Delta\cos(t)}{1 + \Delta\sin(t)}x. \tag{2.25}$$

For the lateral boundaries, (2.6)–(2.9) become

$$h(0, t) = 1, \tag{2.26}$$

$$h_x(a(t), t) = 0, \tag{2.27}$$

$$u(0, y, t) = v(0, y, t) = 0, \tag{2.28}$$

$$Q = (u_{wall}h)|_{x=a(t)}. \tag{2.29}$$

The boundary conditions (2.10), (2.11) and (2.12) at the interface $y = h(x, t)$ become

$$h_t + uh_x - v = 0, \tag{2.30}$$

$$-p + \frac{2\varepsilon^2}{(1 + \varepsilon^2 h_x^2)}\left[\varepsilon^2 u_x h_x^2 - \varepsilon h_x(u_y + \varepsilon^2 v_x) + v_y\right] = \frac{\varepsilon^2}{Ca}\kappa(1 - M(\hat{\Gamma} - \hat{\Gamma}_0)), \tag{2.31a}$$

$$\sigma = 1 - M(\hat{\Gamma} - \hat{\Gamma}_0), \tag{2.31b}$$

$$\frac{1}{(1 + \varepsilon^2 h_x^2)}\left[(1 - \varepsilon^2 h_x^2)(u_y + \varepsilon^2 v_x) + 2\varepsilon^2 h_x(v_y - u_x)\right] = -\frac{\varepsilon M}{Ca(1 + \varepsilon^2 h_x^2)^{1/2}}\hat{\Gamma}_x, \tag{2.32}$$

where κ is the interfacial curvature and the Marangoni number $M = -(\Gamma_\infty^*/\sigma_0^*) \times (\partial\sigma^*/\partial\Gamma^*)_0$. Notice that calculated κ using planar geometry does not capture the circumferential component that may cause drainage for more realistic alveolar geometry. In order to assess this effect we derive κ:

$$\kappa = 1 + \varepsilon(h_{xx} + h) + O(\varepsilon^2). \tag{2.33}$$

When the fluid layer is thin, the above is equivalent to the curvature transformed from that in polar coordinates. The constant curvature part can be absorbed by redefining pressure. For (2.33), the second term is the same as that in planar geometry and the third term arises from the circumferential curvature due to alveolar geometry.

Let us discuss the validity of the dimensionless equation of state, (2.31*b*). As mentioned for (2.13), the surfactant concentration could be high in a normal lung or low in a diseased lung. Estimation from the equation of state for pulmonary surfactant DPPC measured by Schurch *et al.* (1989) suggests that, $M = O(1)$ for $\hat{\Gamma} < 0.2$, and $M = O(10^{-2}) \sim O(10^{-3})$ for $\hat{\Gamma} > 0.8$. It is worth noting that the surfactant activity is expected to be small when the surfactant concentration is close to the maximum packing concentration. As we shall show later, we can develop scaling analysis and a model to capture mechanisms working in both low and high surfactant concentration regimes.

The evolution for the surfactant transport along the interface becomes

$$\hat{\Gamma}_t + \frac{\partial}{\partial x}\left(\frac{\hat{\Gamma}(u + \varepsilon^2 v h_x)}{(1 + \varepsilon^2 h_x^2)}\right) + \frac{\hat{\Gamma}(u + \varepsilon^2 v h_x) h_x h_{xx} \varepsilon^3}{(1 + \varepsilon^2 h_x^2)^2}$$

$$- \frac{1}{Pe_s(1 + \varepsilon^2 h_x^2)} \frac{\partial}{\partial x}\left(\frac{1}{(1 + \varepsilon^2 h_x^2)} \hat{\Gamma}_x\right) + \frac{\hat{\Gamma}\kappa\varepsilon^2(-u h_x + v)}{(1 + \varepsilon^2 h_x^2)^{1/2}} = \hat{J}, \tag{2.34}$$

where $Pe_s = \omega a_0^2/D_s$ is the surface Péclet number. The dimensionless surface flux $\hat{J} = J^*/\omega\Gamma_\infty^*$ is

$$\hat{J} = K(\hat{C}_s - \hat{\Gamma}) = -\frac{1}{\beta\varepsilon^2 Pe_b} \frac{(\hat{C}_y - \varepsilon^2 h_x \hat{C}_x)_{y=h}}{(1 + \varepsilon^2 h_x^2)^{1/2}}, \tag{2.35}$$

where $K = k_2/\omega$ is the ratio of the cycle to the desorption time scales, $Pe_b = \omega a_0^2/D_b$ is the bulk Péclet number, and $\beta = k_1/(k_2 d)$ is the ratio of desorption to adsorption time scales and represents the solubility of the surfactant. Note that β depends on the thickness of the fluid layer. For larger β, the surfactant tends to be more insoluble because it has more difficulty being desorbed into the bulk.

The dimensionless governing equation for bulk concentration is

$$\varepsilon^2 Pe_b(\hat{C}_t + u\hat{C}_x + v\hat{C}_y) = \varepsilon^2 \hat{C}_{xx} + \hat{C}_{yy}, \tag{2.36}$$

and is subject to the boundary conditions:

$$\hat{C}_x(0, y, t) = \hat{C}_x(a(t), y, t) = 0. \tag{2.37}$$

The global constraints for fluid volume and amount of surfactant are

$$\int_0^{a(t)} h(x, t)\, \mathrm{d}x = V_0, \tag{2.38}$$

$$\int_0^{a(t)} \hat{\Gamma}(x,t)\,\mathrm{d}s + \frac{1}{\beta}\int_0^{a(t)}\int_0^{h(x,t)} \hat{C}(x,y,t)\,\mathrm{d}y\,\mathrm{d}x = M_s, \tag{2.39}$$

where V_0 and M_s are now scaled by $a_0 d$ and $\Gamma_\infty^* a_0$, respectively.

We now perform a scaling analysis to further simplify this model. Because Re is very small, inertia is negligible and the system is governed by the Stokes flow. We establish the scalings based on the core region as follows. Since the liquid layer is thin compared with the width of the system ($\varepsilon \ll 1$), the viscous stress u_{yy} dominates in the x-momentum in (2.23a). For small Ca, capillarity usually dominates the normal stress condition. In this case, the pressure is provided by capillarity due to the deformation of the interface. The normal stress condition (2.31) (after redefining p) gives $p \sim \varepsilon^3/Ca$ at leading order. Note that the presence of surfactants can affect (via $M(\hat{\Gamma}-\hat{\Gamma}_0)$) the surface tension σ for the capillary pressure. As we shall show below, the surfactant effect on changing the surface tension is of higher order as long as $M(\hat{\Gamma}-\hat{\Gamma}_0) \ll 1$. Balancing the viscous stress u_{yy} with p_x in (2.23a) yields $Ca \sim \varepsilon^3$ which means surface tension effects are strong.

A balance between the viscous shear and the Marangoni stress from the tangential stress condition, (2.32), gives $\varepsilon^{-1}u_y \sim -(M/Ca)\hat{\Gamma}_x$. This results in $M\hat{\Gamma} \sim \varepsilon^2$ for $Ca \sim \varepsilon^3$. As a result, the variation of the surface tension due to the presence of surfactant is $O(\varepsilon^2)$ and is thus negligible at leading order. $M\hat{\Gamma} \sim \varepsilon^2$ leads to two possible selections of scalings involving surfactant concentration: (i) $\hat{\Gamma} \sim \varepsilon^2$ and $M \sim O(1)$, or (ii) $\hat{\Gamma} \sim O(1)$ and $M \sim O(\varepsilon^2)$. As in the earlier discussion for the equation of state (2.31b), estimation from the equation of state for pulmonary surfactant DPPC measured by Schurch *et al.* (1989) suggests that, $M = O(1)$ for $0 < \hat{\Gamma} < 0.2$, which is suitable for the scaling option (i), and $M = O(10^{-3}) \sim O(10^{-2})$ for $0.8 < \hat{\Gamma} < 1$, which works for the scaling option (ii), and allows our analysis to be used for either normal or low surfactant concentrations.

Let us first complete the scaling analysis in the low $\hat{\Gamma}$ regime. For $\hat{\Gamma} \sim \varepsilon^2$ and $M \sim O(1)$, (2.34) for $\hat{\Gamma}$ yields the surface flux $\hat{J} \sim \varepsilon^2$. If the bulk diffusion acts rapidly across the thin layer (i.e. $\varepsilon^2 Pe_b \ll 1$), then the bulk concentration $\hat{C}$ from (2.36) is independent of y at leading order. As a result, the surface flux is kinetic-controlled for $\beta \sim O(1)$ and $\hat{C}_s$ can be replaced by $\hat{C}$. Therefore, for $K \sim O(1)$ and $\hat{J} \sim \varepsilon^2$, $\hat{C} \sim \varepsilon^2$.

Similarly, for the $O(1)\,\hat{\Gamma}$ regime, $\hat{\Gamma} \sim O(1)$ and $M \sim O(\varepsilon^2)$ yield $\hat{J} \sim O(1)$ and $\hat{C} \sim O(1)$ when $\beta \sim O(1)$ and $K \sim O(1)$. Accordingly, as we shall see later, the model formulations for both scalings are identical.

We should make a few comments on the above scalings. They are based on the balance between the capillary force, the Marangoni force, and the alveolar wall's stretching motion. They work in either the low or $O(1)\,\hat{\Gamma}$ regime. In the $O(1)\,\hat{\Gamma}$ regime, however, the capillary force may be weak owing to a low surface tension, i.e. $Ca \gg \varepsilon^3$. In this case, just as in the previous studies (Podgorski & Gradon 1993; Espinosa & Kamm 1997), only the Marangoni effect and the wall's stretching motion play dominant roles in determining the flow. As a result, $M\hat{\Gamma} \sim \varepsilon^{-1}Ca \gg \varepsilon^2$ that is applicable for a wider $\hat{\Gamma}$ regime. However, when $\hat{\Gamma}$ is very close to 1, a more realistic equation of state rather than (2.13) should be used. Further, the sorptive kinetics model used in (2.15) is no longer appropriate and more sophisticated sorptive models should be incorporated (Espinosa & Kamm 1997; Krueger & Gaver 2000).

The present analysis not only works in the high-tension regime, but also can extend to the low-tension regime, particularly for relatively high surfactant concentration. Since most previous studies are focused on the low-tension regime, we thus devote

our efforts to the analysis for the high-tension regime and discuss results compared to those for the low-tension regime in § 5.3.

3. The outer (core) flow

For the scalings in the low $\hat{\Gamma}$ regime, we let $Ca = \hat{C}a\varepsilon^3$, where $\hat{C}a$ is $O(1)$, and rescale variables by letting

$$(\hat{\Gamma}, \hat{C}, \hat{J}) = (\varepsilon^2\Gamma, \varepsilon^2 C, \varepsilon^2 J). \tag{3.1}$$

The leading-order governing equations for fluid motion become

$$u_x + v_y = 0, \tag{3.2}$$

$$-p_x + u_{yy} = O(\varepsilon^2), \tag{3.3a}$$

$$p_y = O(\varepsilon^2). \tag{3.3b}$$

Equations (3.2) and (3.3) can be solved in conjunction with the following leading-order boundary conditions at the membrane wall and the interface:

$$u = u_{wall}, \quad v = 0 \quad \text{at } y = 0, \tag{3.4}$$

$$p = -\frac{1}{\hat{C}a}(h_{xx} + h) + O(\varepsilon^2) \quad \text{at } y = h, \tag{3.5}$$

$$u_y = -\frac{M}{\hat{C}a}\Gamma_x + O(\varepsilon) \quad \text{at } y = h. \tag{3.6}$$

At leading order, (3.5) is a linearized Young–Laplace equation. The leading-order pressure is thus provided by the interfacial deformation with the linearized curvature $h + h_{xx}$. Also, because of (3.3*b*), the pressure remains unchanged across the fluid layer. Thus, a capillary pressure difference due to locally different curvatures of the interface can drive flows. For (3.6), the Marangoni stress is proportional to the surface concentration gradient because a linear equation of state is assumed. The solutions to u and v are given by

$$u = p_x\left(\tfrac{1}{2}y^2 - hy\right) - \frac{M}{\hat{C}a}\Gamma_x y + u_{wall}, \tag{3.7a}$$

$$v = -p_{xx}\left(\tfrac{1}{6}y^3 - \tfrac{1}{2}hy^2\right) + p_x h_x \tfrac{1}{2}y^2 + \frac{M}{\hat{C}a}\Gamma_{xx}\tfrac{1}{2}y^2 - u_{wall,x}y. \tag{3.7b}$$

where p is given by (3.5). As a result, the flow fields (3.7) consist of three types of flow mechanism: capillary-driven flow, Marangoni flow, and the flow due to the stretching of the bottom wall. Notice that (3.7*b*) generally does not satisfy the no-slip condition (2.28) at the boundary $x = 0$. Substituting (3.7) and (3.5) into the kinematic condition (2.30) yields the following interfacial evolution equation:

$$h_t + \left(\frac{1}{3\hat{C}a}h^3(h_{xxx} + h_x) - \frac{M}{2\hat{C}a}h^2\Gamma_x + u_{wall}h\right)_x = 0. \tag{3.8}$$

Similarly, the interfacial transport of the surfactant (2.34) becomes

$$\Gamma_t + \left(\frac{1}{2\hat{C}a}\Gamma h^2(h_{xxx} + h_x) - \frac{M}{\hat{C}a}h\Gamma\Gamma_x + u_{wall}\Gamma - \frac{1}{Pe_s}\Gamma_x\right)_x - J = 0. \tag{3.9}$$

Note that, in the thin film limit of (2.34), the variation of the surface concentration due to the interfacial curvature is a higher-order effect ($O(\varepsilon^2)$). Although our present model neglects the effect due to the alveolar curvature on the conservation of the fluid, (3.8), and surfactant mass, (3.9), the terms $u_{wall}h$ of (3.8) and $u_{wall}\Gamma$ of (3.9) reflect the effects due to the variation of the circumference of an alveolus on the fluid and surfactant mass, respectively. They indeed have similar impacts to the corresponding terms for the curvature effects in a spherical model studied by Podgorski & Gradon (1993).

The diffusive flux from the bulk is

$$J = -\frac{1}{\beta Pe_b}(C_y - \varepsilon^2 h_x C_x)_{y=h} + O(\varepsilon^4). \tag{3.10}$$

When the vertical diffusion is very rapid such that $\varepsilon^2 Pe_b \ll 1$ as in Jensen & Grotberg (1993), the bulk concentration can be expanded in powers of $\varepsilon^2 Pe_b$:

$$C(x, y, t) = C_0(x, t) + \varepsilon^2 Pe_b C_1(x, y, t) + \cdots. \tag{3.11}$$

Note that the leading order C_0 is independent of y. Since the original scaling of the bulk concentration is $O(\varepsilon^2)$, the correction due to weak convection is actually $O(\varepsilon^4 Pe_b)$. Substituting (3.11) into (3.10) and relating the sorption kinetics gives

$$J = -\frac{1}{\beta}\left(C_{1,y} - \frac{1}{Pe_b}h_x C_{0,x}\right)_{y=h} = K(C_0 - \Gamma)_{y=h}. \tag{3.12}$$

We then substitute (3.11) into (2.36) for the bulk concentration. This results in

$$C_{0,t} + uC_{0,x} = \frac{1}{Pe_b}C_{0,xx} + C_{1,yy} + O(\varepsilon^2 Pe_b, \varepsilon^2). \tag{3.13}$$

Because (3.13) involves the next order $C_1(x, y, t)$, we follow the approach as in Jensen & Grotberg (1993) by taking the cross-sectional average for the concentration. Define the cross-sectional average $\tilde{A}$ of quantity A as $\tilde{A} \equiv (1/h)\int_0^h A\,\mathrm{d}y$. Taking the cross-sectional average for (3.13) yields

$$C_{0,t} + \tilde{u}C_{0,x} = \frac{1}{hPe_b}(hC_{0,x})_x - \frac{1}{hPe_b}h_x C_{0,x}\bigg|_{y=h} + \frac{1}{h}C_{1,y}\bigg|_{y=h} - \frac{1}{h}C_{1,y}\bigg|_{y=0}, \tag{3.14}$$

where $\tilde{u}(x, t) = (1/3\hat{C}a)h^2(h_{xxx}+h_x)-(M/2\hat{C}a)h\Gamma_x+u_{wall}$ is the cross-sectional average velocity in the x-direction. The impermeable condition at the membrane wall requires $C_{1,y|_{y=0}} = 0$. We use (3.12) to relate J with the second and third terms on the right-hand side of (3.14). Letting $C_0 = c$ for simplicity, we derive the following evolution equation for the (cross-sectional averaged) bulk concentration:

$$c_t + \left(\frac{1}{3\hat{C}a}h^2(h_{xxx} + h_x) - \frac{M}{2\hat{C}a}h\Gamma_x + u_{wall}\right)c_x - \frac{1}{hPe_b}(hc_x)_x + \frac{J\beta}{h} = 0. \tag{3.15}$$

Therefore, a system of coupled equations (3.8), (3.9) and (3.15) govern the interfacial evolution, the surface concentration and the bulk concentration, respectively. The flux of the surfactant at the interface J is given by (3.12). These equations are subject to

the following boundary conditions:

$$h(0,t)=1, \quad h_x(a(t),t)=0, \tag{3.16}$$

$$(h_{xxx}+h_x)|_{x=0}=0, \quad h_{xxx}(a(t),0)=0, \tag{3.17a,b}$$

$$\Gamma_x(0,t)=0, \quad \Gamma_x(a(t),t)=0, \tag{3.18a,b}$$

$$c_x(0,t)=0, \quad c_x(a(t),t)=0. \tag{3.19}$$

Note that (3.17*b*) and (3.18*b*) are required to satisfy (2.9) owing to the constant volume constraint. In addition, for the global constraints of surfactant mass, we should let $M_s \to \varepsilon^2 M_s$ for (2.39) based on the scalings (3.1). The system is at equilibrium when it is not stretching (i.e. $\Delta = 0$). This leads to $c = \Gamma = 1$. Thus, (2.38) and (2.39) require $M_s = 1 + (V_0/\beta)$.

For the $O(\varepsilon^2)$ $\hat{\Gamma}$ regime, we have derived the above system of coupled evolution equations that dictate the behaviour of the liquid film, the surface surfactant distributions, and the bulk concentration for the flow in the central core region. Similar derivation procedures for the $O(1)$ $\hat{\Gamma}$ regime with $(\hat{\Gamma}, \hat{C}, \hat{J}, M) \to (\Gamma, C, J, \varepsilon^2 M)$ can derive an identical set of equations and boundary conditions.

To examine the response in the limit of small strain amplitude Δ, we expand

$$\left.\begin{aligned} h(x,t) &= h_0(x,t) + \Delta h_1(x,t) + \Delta^2 h_2(x,t) + O(\Delta^3), \\ \Gamma(x,t) &= \Gamma_0(x,t) + \Delta \Gamma_1(x,t) + \Delta^2 \Gamma_2(x,t) + O(\Delta^3), \\ c(x,t) &= c_0(x,t) + \Delta c_1(x,t) + \Delta^2 c_2(x,t) + O(\Delta^3). \end{aligned}\right\} \tag{3.20}$$

We substitute these expressions into the governing equations and boundary conditions and solve a problem at each order in Δ. Because we are interested in cycle-averaged quantities, as we shall see later, in order to obtain a non-zero cycle average, it is necessary to solve the problem up to $O(\Delta^2)$. Therefore, we must assume $\Delta^2 \gg \varepsilon$ in order for the expansions to remain valid up to $O(\Delta^2)$ at the leading order in ε.

3.1. The $O(\Delta^0)$ problem

At $O(\Delta^0)$, since the wall motion represents the only driving force in the problem, the system remains static. Any temporal transitions at this order are due to non-equilibrium initial conditions for the interface shape or surfactant concentration. We do not consider this transition and take this static state as the base state. Therefore, the pressure is purely hydrostatic, i.e. no capillary pressure gradient, and uniform surfactant distribution. Thus, (3.8) reduces to the following equation governing the static interface:

$$h_{0,xxx} + h_{0,x} = 0, \tag{3.21}$$

with

$$h_0(0)=1, \quad h_{0,x}(1)=0, \quad \int_0^1 h_0(x)\,\mathrm{d}x = V_0. \tag{3.22}$$

The solution to (3.21) is

$$\left.\begin{aligned} h_0(x) &= k + (1-k)\cos(x) + \tan(1)(1-k)\sin(x), \\ k &= (V_0 - \tan(1))/(1-\tan(1)). \end{aligned}\right\} \tag{3.23a}$$

When the liquid volume $V_0 = 1$, the interface at this order is flat. It is clear that larger (smaller) V_0 leads the interface to become convex (concave). It is also evident

that the corresponding surfactant concentration is uniform everywhere, i.e.

$$\Gamma_0(x) = c_0(x) = 1. \tag{3.23b}$$

3.2. The $O(\Delta)$ problem

At $O(\Delta)$, the effect of wall motion is introduced. The resulting equations and boundary conditions are expected to be non-homogeneous with terms that are time periodic. Equations (3.8), (3.9) and (3.15) at this order reduce to

$$h_{1,t} + \left(\frac{1}{3\hat{C}a}h_0^3(h_{1,xxx} + h_{1,x}) - \frac{M}{2\hat{C}a}h_0^2\Gamma_{1,x}\right)_x = -(h_0 + xh_{0,x})\cos(t), \tag{3.24}$$

$$\Gamma_{1,t} + \left(\frac{h_0^2}{2\hat{C}a}(h_{1,xxx} + h_{1,x}) - \frac{M}{\hat{C}a}h_0\Gamma_{1,x} - \frac{1}{Pe_s}\Gamma_{1,x}\right)_x - K(c_1 - \Gamma_1) = -\cos(t), \tag{3.25}$$

$$c_{1,t} - \frac{1}{Pe_b h_0}(h_0 c_{1,x})_x + \frac{\beta K}{h_0}(c_1 - \Gamma_1) = 0. \tag{3.26}$$

Note that the convective term of (3.15) does not contribute to (3.26) for the bulk surfactant transport at $O(\Delta)$. The corresponding boundary conditions are

$$\left.\begin{array}{c} h_1(0,t) = 0, \quad h_{1,x}(1,t) = -\sin(t)h_{0,xx}(1), \\ (h_{1,xxx} + h_{1,x})|_{x=0} = 0, \quad h_{1,xxx}(1,t) = -\sin(t)h_{0,xxxx}(1), \\ \Gamma_{1,x}(0,t) = 0, \quad \Gamma_{1,x}(1,t) = 0, \\ c_{1,x}(0,t) = 0, \quad c_{1,x}(1,t) = 0. \end{array}\right\} \tag{3.27}$$

The volume and surfactant mass constraints are

$$\int_0^1 h_1(x,t)\,\mathrm{d}x = -\sin(t)h_0(x=1), \qquad \int_0^1 \Gamma_1(x,t)\,\mathrm{d}x + \frac{1}{\beta}\int_0^1 h_0(x)c_1(x,t)\,\mathrm{d}x = -\sin(t). \tag{3.28}$$

Because we are interested only in the long-time response to the wall's temporally periodic stretching, the homogeneous solutions corresponding to initial transition states are not considered here. Observing (3.24)–(3.28) whose inhomogeneous terms are proportional to $\sin(t)$ or $\cos(t)$, the solutions can be thus expressed as:

$$\left.\begin{array}{l} h_1(x,t) = A(x)\cos(t) + B(x)\sin(t), \\ \Gamma_1(x,t) = D(x)\cos(t) + E(x)\sin(t), \\ c_1(x,t) = R(x)\cos(t) + S(x)\sin(t). \end{array}\right\} \tag{3.29}$$

Substituting (3.29) into (3.24)–(3.26) produces a system of coupled ordinary differential equations for unknown coefficients A, B, D, E, R and S. We solve them by using a shooting method in conjunction with a multi-dimensional root finder. The corresponding velocities are

$$u_1 = \frac{1}{\hat{C}a}(h_{1,xxx} + h_{1,x})\left(h_0 y - \tfrac{1}{2}y^2\right) - \frac{M}{\hat{C}a}\Gamma_{1,x}y + x\cos(t), \tag{3.30a}$$

$$v_1 = \frac{1}{\hat{C}a}(h_{1,xxxx} + h_{1,xx})\left(\tfrac{1}{6}y^3 - \tfrac{1}{2}h_0 y^2\right) - \frac{1}{\hat{C}a}(h_{1,xxx} + h_{1,x})h_{0,x}\frac{y^2}{2} + \frac{M}{\hat{C}a}\Gamma_{1,xx}\frac{y^2}{2} - y\cos(t). \tag{3.30b}$$

However, because of (3.29), the solutions for the $O(\Delta)$ problem contribute to zero cycle averages and we have to solve the problem at order Δ^2.

3.3. *The $O(\Delta^2)$ problem and cycle-averaged quantities*

For the $O(\Delta^2)$ problem, recall that we assume $\Delta^2 \gg \varepsilon$ in order to have valid expansions. The evolution equations (3.8), (3.9) and (3.15) become

$$h_{2,t} + \left(\frac{1}{3\hat{C}a}h_0^3(h_{2,xxx} + h_{2,x}) - \frac{M}{2\hat{C}a}h_0^2\Gamma_{2,x}\right)_x = -\left(\frac{h_0^2}{\hat{C}a}h_1(h_{1,xxx} + h_{1,x}) - \frac{2M}{\hat{C}a}h_0h_1\Gamma_{1,x} + x\cos(t)(h_1 - h_0\sin(t))\right)_x, \quad (3.31)$$

$$\Gamma_{2,t} + \left(\frac{h_0^2}{2\hat{C}a}(h_{2,xxx} + h_{2,x}) - \left(\frac{M}{\hat{C}a}h_0 + \frac{1}{Pe_s}\right)\Gamma_{2,x}\right)_x - K(c_2 - \Gamma_2) = -\left(\frac{h_0}{\hat{C}a}h_1(h_{1,xxx} + h_{1,x}) + \frac{h_0^2}{2\hat{C}a}\Gamma_1(h_{1,xxx} + h_{1,x}) - \frac{M}{\hat{C}a}(\Gamma_1\Gamma_{1,x} + h_0h_1\Gamma_{1,x}) + x\cos(t)(\Gamma_1 - \sin(t))\right)_x, \quad (3.32)$$

$$c_{2,t} - \frac{1}{Pe_bh_0}(h_0c_{2,x})_x + \frac{\beta K}{h_0}(c_2 - \Gamma_2) = -c_{1,x}\left(\frac{h_0^2}{3\hat{C}a}(h_{1,xxx} + h_{1,x}) - \frac{M}{2\hat{C}a}h_0\Gamma_{1,x} + x\cos(t)\right) + \frac{1}{Pe_b}\left(\frac{1}{h_0}h_{1,x}c_{1,x} - \frac{h_{0,x}}{h_0^2}h_1c_{1,x}\right) + \frac{\beta K}{h_0^2}h_1(c_1 - \Gamma_1). \quad (3.33)$$

The boundary conditions at this order are

$$\left.\begin{gathered} h_2(0,t) = 0, \quad h_{2,x}(1,t) = -\sin(t)h_{1,xx}(1,t) - \tfrac{1}{2}\sin^2(t)h_{0,xxx}(1), \\ (h_{2,xxx} + h_{2,x})|_{x=0} = 0, \quad h_{2,xxx}(1,t) = -\sin(t)h_{1,xxxx}(1,t) - \tfrac{1}{2}\sin^2(t)h_{0,xxxxx}(1), \\ \Gamma_{2,x}(0,t) = 0, \quad \Gamma_{2,x}(1,t) = -\sin(t)\Gamma_{1,xx}(1,t), \\ c_{2,x}(0,t) = 0, \quad c_{2,x}(1,t) = -\sin(t)c_{1,xx}(1,t). \end{gathered}\right\} \quad (3.34)$$

Similarly, the volume and surfactant mass constraints are

$$\left.\begin{gathered} \int_0^1 h_2(x,t)\,\mathrm{d}x = -\sin(t)h_1(1,t), \\ \int_0^1 \Gamma_2(x,t)\,\mathrm{d}x + \sin(t)\Gamma_1(1,t) \\ + \frac{1}{\beta}\left(\int_0^1 h_0(x)c_2(x,t)\,\mathrm{d}x + \int_0^1 h_1(x)c_1(x,t)\,\mathrm{d}x + \sin(t)h_0(x)c_1(1,t)\right) = 0. \end{gathered}\right\} \quad (3.35)$$

To determine the induced, steady-streaming at this order, we average the above equations and boundary conditions over a period of the oscillation. The cycle averages for terms containing $\cos(t)\sin(t)$ are zero, but those for $\cos^2(t)$ or $\sin^2(t)$ are non-zero and produce net steady quantities. The terms $\overline{h}_2(x)$, $\overline{\Gamma}_2(x)$, and $\overline{c}_2(x)$ (where overbars indicate cycle-averaged quantities) are determined by using the same numerical techniques as in the first-order problem. The cycle-averaged velocity components

at this order are

$$\overline{u}_2 = -\frac{1}{\hat{C}a}(\overline{h}_{2,xxx} + \overline{h}_{2,x})\left(\tfrac{1}{2}y^2 - h_0 y\right) + \frac{1}{\hat{C}a}\overline{(h_1(h_{1,xxx} + h_{1,x}))}y - \frac{M}{\hat{C}a}\overline{\Gamma}_{2,x}y, \quad (3.36a)$$

$$\overline{v}_2 = \frac{1}{\hat{C}a}(\overline{h}_{2,xxxx} + \overline{h}_{2,xx})\left(\tfrac{1}{6}y^3 - \tfrac{1}{2}h_0 y^2\right) - \frac{h_{0,x}}{\hat{C}a}(\overline{h}_{2,xxx} + \overline{h}_{2,x})\left(\tfrac{1}{2}y^2\right)$$

$$-\overline{(h_1(h_{1,xxx} + h_{1,x}))_x}\frac{y^2}{2\hat{C}a} + \frac{M}{\hat{C}a}\overline{\Gamma}_{2,xx}\tfrac{1}{2}y^2. \quad (3.36b)$$

Note that the cycle-averaged flow fields (3.36) do not contain the wall's stretching motions since $\overline{u_{wall}}$ is zero. However, the stretching motions have an explicit impact on the $O(\Delta)$ flow fields on which those of $O(\Delta^2)$ depend.

4. The inner (boundary-layer) flow near the pinned wall

The core flow as shown in the previous section is only valid for the region where the horizontal length scale is much longer that the vertical one. For the fluid near the pinned wall where both length scales are comparable, its motion should be otherwise analysed.

In this region, the characteristic length scale should be the wall's height d. The corresponding velocity scale is ωd. As such, we rescale the length scales and velocities in both x- and y-directions, and the pressure by

$$X = x/\varepsilon, \quad Y = y. \quad (4.1)$$

$$U = u/\varepsilon, \quad V = v, \quad P = p/\varepsilon^2. \quad (4.2)$$

For surfactant transport quantities, we let $\tilde{\tilde{\Gamma}}$, $\tilde{\tilde{C}}$ and $\tilde{\tilde{J}}$ denote the surface concentration, the bulk concentration and the diffusive flux in the inner region, respectively. Note that $\tilde{\tilde{\Gamma}}$, $\tilde{\tilde{C}}$ and $\tilde{\tilde{J}}$ should be scaled by ε^2 just as in the outer region. We then let $(\tilde{\tilde{\Gamma}}, \tilde{\tilde{C}}, \tilde{\tilde{J}}) = (\varepsilon^2\tilde{\Gamma}, \varepsilon^2\tilde{C}, \varepsilon^2\tilde{J})$. The governing equations for the fluid motion become

$$U_X + V_Y = 0, \quad (4.3)$$

$$Re\,\varepsilon^2[U_t + UU_X + VU_Y] = -P_X + U_{XX} + U_{YY}, \quad (4.4a)$$

$$Re\,\varepsilon^2[V_t + UV_X + VV_Y] = -P_Y + V_{XX} + V_{YY}. \quad (4.4b)$$

Note that $Re\,\varepsilon^2 = \rho\omega d^2/\mu$ should be recognized as the Reynolds number for the inner region. The associated boundary conditions at the wall are

$$U = V = 0 \quad \text{at } X = 0, \quad (4.5)$$

and

$$U = \frac{\Delta\cos(t)}{1 + \Delta\sin(t)}X, \quad V = 0 \quad \text{at } Y = 0. \quad (4.6)$$

At the interface $Y = H(X, t)$, the kinematic, normal stress and tangential stress boundary conditions become

$$V = H_t + UH_X, \quad (4.7)$$

$$-P + \frac{2}{(1 + H_X^2)}\left[U_X H_X^2 - H_X(U_Y + V_X) + V_Y\right] = \frac{\kappa}{\varepsilon Ca}[1 - \varepsilon^2 M\tilde{\Gamma}], \quad (4.8)$$

$$\frac{1}{(1 + H_X^2)}\left[(1 - H_X^2)(U_Y + V_X) + 2H_X(V_Y - U_X)\right] = -\frac{\varepsilon^2 M}{\varepsilon Ca(1 + H_X^2)^{1/2}}\tilde{\Gamma}_X. \quad (4.9)$$

Again, $\varepsilon Ca = \mu\omega d/\sigma_0^*$ is the capillary number for the inner region. The surfactant transport equation along the interface becomes

$$\tilde{\Gamma}_t + \left(\frac{\tilde{\Gamma}(U + VH_X)}{(1+H_X^2)}\right)_X - \frac{1}{\varepsilon^2 Pe_s}\tilde{\nabla}_s^2\tilde{\Gamma} + \frac{\tilde{\Gamma}\kappa(-UH_X + V)}{(1+H_X^2)^{1/2}} = \tilde{J}, \tag{4.10}$$

and

$$\tilde{J} = K(\tilde{C}_s - \tilde{\Gamma}) = -\frac{1}{\beta\varepsilon^2 Pe_b}\frac{(\tilde{C}_Y - H_X\tilde{C}_X)}{(1+H_X^2)^{1/2}}, \tag{4.11}$$

where $\varepsilon^2 Pe_s = \omega d^2/D_s$ and $\varepsilon^2 Pe_b = \omega d^2/D_b$ are the surface and the bulk Péclet numbers, respectively, for the inner region. Recall that $\varepsilon^2 Pe_b \ll 1$ has been assumed for deriving the evolution equation of the bulk concentration (3.15) in the outer core region. The required boundary condition for $\tilde{\Gamma}$ is

$$\tilde{\Gamma}_X(X = 0) = 0. \tag{4.12}$$

The appropriate matching conditions are

$$\lim_{X\to\infty} \varepsilon U = \lim_{x\to 0} u, \quad \lim_{X\to\infty} V = \lim_{x\to 0} v \quad \text{as } \varepsilon \to 0, \tag{4.13a,b}$$

$$\lim_{X\to\infty} \tilde{\Gamma} = \lim_{x\to 0} \Gamma \quad \text{as } \varepsilon \to 0. \tag{4.14}$$

For the concentration $\tilde{C}$ in the inner region, the equation is

$$Pe_b\varepsilon^2[\tilde{C}_t + V\tilde{C}_X + V\tilde{C}_Y] = \tilde{C}_{XX} + \tilde{C}_{YY}. \tag{4.15}$$

The boundary conditions and matching conditions are

$$\tilde{C}_Y(Y = 0) = 0, \tag{4.16}$$

$$K(\tilde{C}_s - \tilde{\Gamma}) = -\frac{1}{\beta\varepsilon^2 Pe_b}\frac{(\tilde{C}_Y - H_X\tilde{C}_X)}{(1+H_X^2)^{1/2}} \quad \text{at } Y = H, \tag{4.17}$$

$$\tilde{C}_X(X = 0) = 0, \tag{4.18}$$

$$\lim_{X\to\infty} \tilde{C} = \lim_{x\to 0} C \quad \text{as } \varepsilon \to 0. \tag{4.19}$$

With the above general formulation for the inner region, we now begin to consider the leading-order solution. Since we are interested in the leading-order cycle-averaged flow, as we shall show below, we start with an unsteady problem to derive required boundary and matching conditions for the cycle-averaged inner flow field.

At the leading order in ε, we now introduce Ψ as the stream function in the inner region. Then the fluid motion is governed by the biharmonic equation:

$$\tilde{\nabla}^4\Psi = 0 \tag{4.20}$$

where $U = \Psi_Y$, $V = -\Psi_X$ and $\tilde{\nabla}^2 = \partial^2/\partial X^2 + \partial^2/\partial Y^2$. The boundary condition at $Y = 0$ is still (4.6). Note that the cycle-averaged $\overline{U}(Y = 0) = 0$. For the boundary conditions at the interface, the scaling $Ca \sim \varepsilon^3$ leads (4.8) to

$$\kappa = 0, \tag{4.21}$$

with boundary condition and matching conditions

$$H(X = 0) = 1, \tag{4.22}$$

$$\lim_{X\to\infty} H = \lim_{x\to 0} h = 1 \quad \text{as } \varepsilon \to 0. \tag{4.23}$$

The solution is

$$H = 1. \tag{4.24}$$

Thus, the leading-order interface remains flat throughout the inner region. It immediately follows from (4.7) that

$$V(Y = H) = 0. \tag{4.25}$$

Similarly, for $\tilde{\Gamma} \sim O(1)$, $Ca \sim \varepsilon^3$ and $M \sim O(1)$, the Marangoni stress dominates in (4.9) at leading order:

$$\tilde{\Gamma}_X = 0. \tag{4.26}$$

Applying (4.14) leads to the solution

$$\tilde{\Gamma} = \tilde{\Gamma}(t) \equiv \Gamma(x \to 0, t). \tag{4.27}$$

Thus, the leading-order surface concentration is spatially uniform in the inner region. It is just the inner limit of the outer surface concentration. Along with (4.24) and (4.27), (4.10) and (4.11) become

$$\tilde{\Gamma}_t + U_X|_{Y=1}\tilde{\Gamma} = \tilde{J}. \tag{4.28}$$

$$\tilde{J} = K(\tilde{C} - \tilde{\Gamma})_{Y=1} = -\frac{1}{\beta\varepsilon^2 Pe_b}\tilde{C}_Y|_{Y=1}. \tag{4.29}$$

For $\varepsilon^2 Pe_b \ll 1$, the leading order of (4.15) is a steady diffusion equation:

$$\tilde{C}_{XX} + \tilde{C}_{YY} = 0. \tag{4.30}$$

The leading-order boundary condition (4.29) gives the diffusive flux $\tilde{C}_Y(Y = 1) = 0$ at the interface. Since there is also no flux across the wall from (4.16), the resulting concentration does not have a gradient across the liquid layer, namely, $\tilde{C} = \tilde{C}(X, t)$. Solving $\tilde{C}$ from (4.30) with boundary conditions (4.18) and (4.19) yields

$$\tilde{C} = \tilde{C}(t) \equiv C(x \to 0, t). \tag{4.31}$$

As a result, for $\varepsilon^2 Pe_b \ll 1$, the leading-order inner concentration $\tilde{C}$ is simply the inner limit of the outer concentration and is also spatially uniform. Therefore, the surface transport of surfactants (4.28) is again kinetic-controlled, that is

$$\tilde{\Gamma}_t + U_X|_{Y=1}\tilde{\Gamma} = K(\tilde{C} - \tilde{\Gamma}). \tag{4.32}$$

Since both $\tilde{\Gamma}$ and $\tilde{C}$ are functions of time only, (4.32) suggests that

$$U(Y = 1) = G(t)X, \tag{4.33}$$

where $G(t)$ can be, in principle, obtained by matching the outer solution from (4.13*a*) evaluated at the interface. Therefore, taking the cycle-average of (4.33) leads $\overline{G}$ to be a time-independent constant that can be determined from matching with the outer $\overline{u} = \Delta^2\overline{u}_2$.

Now, we can set up the cycle-averaged inner flow problem. Since the outer variables $(\overline{u}, \overline{v}, \overline{\psi})$ are $O(\Delta^2)$, the inner variables $(\overline{U}, \overline{V}, \overline{\Psi})$ should also be $O(\Delta^2)$. Let

$$(\overline{U}, \overline{V}, \overline{\Psi}) = (\Delta^2\overline{U}_2, \Delta^2\overline{V}_2, \Delta^2\overline{\Psi}_2) + O(\Delta^3), \tag{4.34}$$

then the equations for fluid motion are

$$\overline{U}_2 = \overline{\Psi}_{2Y}, \quad \overline{V}_2 = -\overline{\Psi}_{2X}, \tag{4.35a}$$

and

$$\tilde{\nabla}^4 \overline{\Psi}_2 = 0. \tag{4.35b}$$

The boundary conditions are

$$\overline{\Psi}_2 = \overline{\Psi}_{2Y} = 0 \quad \text{at } Y = 0, \tag{4.36}$$

$$\overline{\Psi}_{2Y} = F(1)X, \quad \overline{\Psi}_2 = 0 \quad \text{at } Y = 1, \tag{4.37a,b}$$

$$\overline{\Psi}_{2X} = \overline{\Psi}_2 = 0 \quad \text{at } X = 0, \tag{4.38}$$

with matching conditions

$$\overline{\Psi}_2 \to \overline{\Psi}_{2\infty}, \quad \overline{\Psi}_{2X} \to \overline{\Psi}_{2\infty X} \quad \text{as } X \to \infty, \tag{4.39a,b}$$

where

$$\overline{\Psi}_{2\infty} = \varepsilon^{-1} \overline{\psi}_2(x \to 0) = F(Y)X, \tag{4.40}$$

$$F(Y) = -\frac{(\overline{h}_{2xxxx}(0) + \overline{h}_{2xx}(0))}{\hat{Ca}} \left(\tfrac{1}{6}Y^3 - \tfrac{1}{2}Y^2\right) - \frac{M}{2\hat{Ca}} \overline{\Gamma}_{2xx}(0) Y^2$$
$$= \frac{M}{4\hat{Ca}} \overline{\Gamma}_{2xx}(0)(-Y^3 + Y^2). \tag{4.41}$$

Note that in (4.40), we have used the condition $\overline{v}_2(x \to 0, y = 1) = 0$ from the cycle-averaged evolution equation (3.36*b*) in the outer region to relate $(\overline{h}_{2xxxx} + \overline{h}_{2xx})|_{x=0}$ and $\overline{\Gamma}_{2xx}(0)$:

$$(\overline{h}_{2xxxx} + \overline{h}_{2xx})|_{x=0} = \tfrac{3}{2} M \overline{\Gamma}_{2xx}(0). \tag{4.42}$$

Note that (4.40) also satisfies (4.37) and this is consistent with the matching condition evaluated at $Y = 1$.

It is now sufficient to determine the cycle-averaged inner flow field from (4.35)–(4.39). In view of the matching conditions (4.39), it is convenient to write the solution as

$$\overline{\Psi}_2 = \overline{\Psi}_{2\infty} + \Phi. \tag{4.43}$$

Substituting (4.43) into (4.35)–(4.39) and knowing $\tilde{\nabla}^4 \overline{\Psi}_{2\infty} = 0$ gives

$$\tilde{\nabla}^4 \Phi = 0, \tag{4.44}$$

with boundary conditions

$$\Phi = \Phi_Y = 0 \quad \text{at } Y = 0, \tag{4.45}$$

$$\Phi = \Phi_Y = 0 \quad \text{at } Y = 1, \tag{4.46}$$

$$\Phi_X = -F(Y), \quad \Phi = 0 \text{ at } X = 0. \tag{4.47}$$

The required matching conditions become

$$\Phi \to 0, \quad \Phi_X \to 0 \quad \text{as } X \to \infty. \tag{4.48}$$

To obtain the analytic solution for Φ, we extend a method developed by Benthem (1963) who employed Laplace transform theory. Cormack *et al.* (1974) applied this method for natural convection in a shallow cavity. We change variables by letting

$$Y' = 2Y - 1, \quad X' = 2X. \tag{4.49}$$

We decompose the problem into an even and an odd part, and then add the solutions after solving each part. Let

$$\Phi = \Phi_{even} + \Phi_{odd}. \tag{4.50}$$

The resulting boundary condition (4.47) becomes

$$\Phi_{X'}(X'=0) = (\Phi_{even})_{X'}|_{X'=0} + (\Phi_{odd})_{X'}|_{X'=0}, \tag{4.51}$$

$$(\Phi_{even})_{X'}|_{X'=0} = \frac{M}{8\hat{C}a}\overline{\Gamma}_{2xx}(0)\left(\tfrac{1}{8}Y'^2 - \tfrac{1}{8}\right), (\Phi_{odd})_{X'}|_{X'=0} = \frac{M}{8\hat{C}a}\overline{\Gamma}_{2xx}(0)\left(\tfrac{1}{8}Y'^3 - \tfrac{1}{8}Y'\right).$$

Unlike the situations studied by Benthem (1963) and Cormack *et al.* (1974) whose solutions are only even in Y', our solution for Φ should include both even and odd parts because of $\Phi_{X'}(X'=0)$. Following a similar procedure to Benthem (1963), we expand all derivatives evaluated at $X'=0$ in cosine and sine series for even and odd parts, respectively. The even solution is given by

$$\Phi_{even} = \sum_{k=1}^{\infty}\sum_{n=1}^{\infty} \frac{(2n-1)\pi \sin\left(\frac{1}{2}(2n-1)\pi\right)}{\left(s_k^2 - \frac{1}{4}(2n-1)^2\pi^2\right)^2}$$

$$\times\left(\left(s_k^2 - \tfrac{1}{2}(2n-1)^2\pi^2\right)d_n - s_k a_n + b_n\right) f_{even}(Y', s_k)\exp(-s_k X'). \tag{4.52}$$

where $f_{even}(Y', s) = (\sin(s)\cos(sY') - \cos(s)Y'\sin(sY'))/4\cos^2(s)$ are the even Papkovich–Fadle eigenfunctions (Joseph 1977; Joseph & Sturges 1978). The coefficients d_n, a_n and b_n are defined by the following and the latter two are unknowns.

$$(\Phi_{even})_{X'}|_{X'=0} = \sum_{n=1}^{\infty} d_n \cos\left(\tfrac{1}{2}(2n-1)\pi Y'\right), \tag{4.53a}$$

where

$$d_n = \frac{M}{8\hat{C}a}\overline{\Gamma}_{2xx}(0)\left(\frac{4(-1)^n}{(2n-1)^3\pi^3}\right).$$

$$(\Phi_{even})_{X'X'}|_{X'=0} = \sum_{n=1}^{\infty} a_n \cos\left(\tfrac{1}{2}(2n-1)\pi Y'\right), \tag{4.53b}$$

and

$$(\Phi_{even})_{X'X'X'}|_{X'=0} = \sum_{n=1}^{\infty} b_n \cos\left(\tfrac{1}{2}(2n-1)\pi Y'\right). \tag{4.53c}$$

Here, $s_k\,(k = 1, 2, \ldots, \infty)$ are the complex eigenvalues (with positive real part) determined by the transcendental equation

$$\sin(2s_k) + 2s_k = 0. \tag{4.54}$$

a_n and b_n are determined by the following infinite system of equations:

$$\sum_{n=1}^{\infty} \frac{(2n-1)\pi \sin\left(\frac{1}{2}(2n-1)\pi\right)}{\left(s_k^2 - \frac{1}{4}(2n-1)^2\pi^2\right)^2}\left(\left(s_k^2 - \tfrac{1}{2}(2n-1)^2\pi^2\right)d_n + s_k a_n + b\right) = 0 \quad (k = 1, 2, \ldots, \infty). \tag{4.55}$$

In practice, we must solve them approximately by a truncated matrix. The necessary number of s_k is required and is in order of increasing real part. Furthermore, as pointed out by Cormack *et al.* (1974), the complex conjugate $\overline{s}_k$ of s_k is also the root of (4.54). This guarantees that the imaginary part of the solution is zero.

The odd solution is given by

$$\Phi_{odd} = -\sum_{k=1}^{\infty}\sum_{n=1}^{\infty} \frac{2n\pi\cos(n\pi)}{\left(\hat{s}_k^2 - \frac{1}{4}(2n)^2\pi^2\right)^2}\left(\hat{s}_k^2 - \tfrac{1}{2}(2n)^2\pi^2\hat{d}_n - \hat{s}_k\hat{a}_n + \hat{b}_n\right) f_{odd}(Y', \hat{s}_k)\exp(-\hat{s}_k X'), \tag{4.56}$$

where $f_{odd}(Y', \hat{s}) = (\cos(s)\sin(\hat{s}Y') - \sin(\hat{s})Y'\cos(\hat{s}Y'))/4\sin^2(\hat{s})$ are the odd Papkovich–Fadle eigenfunctions (Joseph 1977; Joseph & Sturges 1978). The coefficients $\hat{d}_n$, $\hat{a}_n$ and $\hat{b}_n$ are defined by the following:

$$(\Phi_{odd})_{X'}|_{X'=0} = \sum_{n=1}^{\infty} \hat{d}_n \sin(n\pi Y'), \tag{4.57a}$$

where

$$\hat{d}_n = \frac{M}{8\hat{C}a}\overline{\Gamma}_{2xx}(0)\left(\frac{3(-1)^n}{2n^3\pi^3}\right),$$

$$(\Phi_{odd})_{X'X'}|_{X'=0} = \sum_{n=1}^{\infty} \hat{a}_n \sin(n\pi Y'), \tag{4.57b}$$

$$(\Phi_{odd})_{X'X'X'}|_{X'=0} = \sum_{n=1}^{\infty} \hat{b}_n \sin(n\pi Y'). \tag{4.57c}$$

The complex eigenvalues $\hat{s}_k$ satisfy

$$\sin(2\hat{s}_k) - 2\hat{s}_k = 0, \tag{4.58}$$

and $\hat{a}_n$ and $\hat{b}_n$ are determined by the following equation in a similar manner to that described for the even part:

$$\sum_{n=1}^{\infty} \frac{2n\pi\cos(n\pi)}{\left(\hat{s}_k^2 - \frac{1}{4}(2n)^2\pi^2\right)^2}\left(\left(\hat{s}_k^2 - \tfrac{1}{2}(2n)^2\pi^2\right)\hat{d}_n - \hat{s}_k\hat{a}_n + \hat{b}_n\right) = 0 \quad (k = 1, 2, \ldots, \infty). \tag{4.59}$$

Combining the even (4.52) and the odd (4.56) solutions gives the solution for Φ, and therefore for $\overline{\Psi}_2$ from (4.43).

5. Results and discussions

5.1. $O(\Delta)$ *unsteady streamlines in the outer (core) region*

As shown in § 3, the flow in the core region is described by lubrication theory. We also expand the problem for small strain amplitude Δ by assuming $\Delta^2 \gg \varepsilon$. The zero order in Δ is just a static state because of no stretching. The stretching motion is then introduced at $O(\Delta)$. Figures 3 and 4 show typical $O(\Delta)$ unsteady streamlines (3.30) during a stretching cycle for insoluble ($K = 0$ or $\beta = \infty$) and soluble surfactants, respectively. Streamlines are drawn in the Eulerian frame. The flow domain is bounded by the wall ($x = 0$ and $y = 0$), the unperturbed interface ($y = h_0 = 1$, here for $V_0 = 1$) and the unperturbed symmetry line ($x = 1$). Notice that the length scales in both the x- and y-directions have been rescaled by a_0 and d, respectively. As a result, curvatures of these streamlines in the middle x-core region, say $x = 0.25 \sim 0.75$, are small and represent almost parallel stream patterns. This is a result of lubrication theory and is only valid in the central core region.

We now turn our attention to the streamline patterns of figures 3 for an insoluble surfactant. We draw eight frames at different time intervals during a stretching cycle. The system expands towards the extensible end until $t = \frac{1}{2}\pi$. For expansions as in $t = 0$

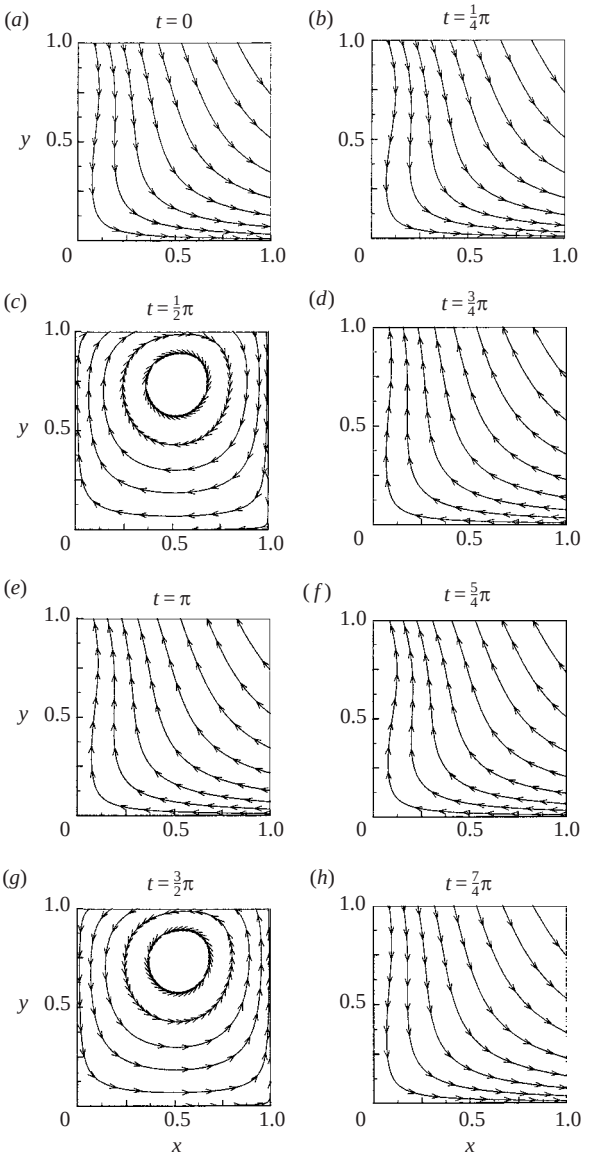

FIGURE 3. The $O(\Delta)$ unsteady streamlines in the presence of an insoluble surfactant. $\hat{C}a = 1$, $M = 1$, $Ps = 10$ and $V_0 = 1$. The streamlines are calculated by (3.30). Note that the true horizontal scale (a_0) is much longer than the vertical one (d). The rigid end (the extensible end) is at $x = 0$ ($x = 1$). The system expands towards the extensible end during $t = 0$ and $t = \frac{1}{2}\pi$. The contraction during $t = 0$ and $t = \frac{3}{2}\pi$ lead the fluid to flow towards the rigid end. The system is then back to the expansion after $t = \frac{3}{2}\pi$.

and $t = \frac{1}{4}\pi$, the streamlines flow towards the symmetry line and the layer thins. At $t = \frac{1}{2}\pi$ the system reaches maximum length, but has zero instantaneous velocity. The streamline shows a clockwise vortex and the fluid flows towards the rigid end. Since there is no normal velocity at $x = 1$ (extensible end) suggested by (3.27) for $h_0 = 1$ at $t = \frac{1}{2}\pi$, the flow must turn around. As we check the flow mechanism at the end of expansion, the surface flow direction is toward the extensible end arising from the

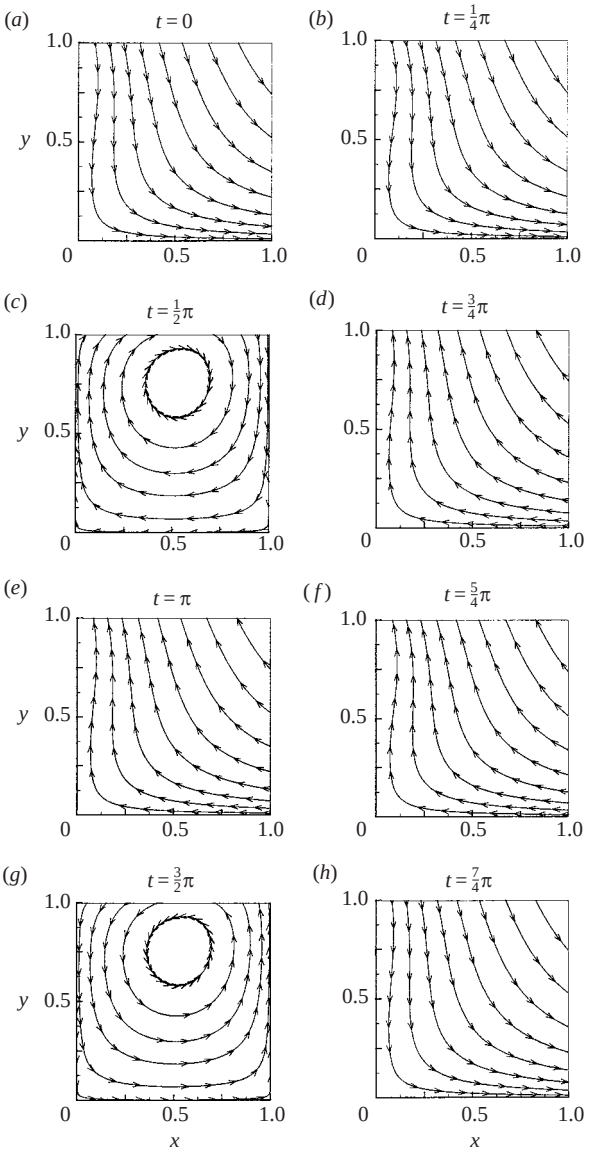

FIGURE 4. The $O(\Delta)$ unsteady streamlines in the presence of a soluble surfactant. $\hat{C}a = 1$, $M = 1$, $Ps = 10$, $Pe_b = 1$, $K = 1$, $\beta = 1$ and $V_0 = 1$. The streamlines are calculated by (3.30). Note that the true horizontal scale (a_0) is much longer than the vertical one (d). The rigid end (the extensible end) is at $x = 0$ ($x = 1$). The system expands towards the extensible end during $t = 0$ and $t = \frac{1}{2}\pi$. The contraction during $t = 0$ and $t = \frac{3}{2}\pi$ leads the fluid to flow towards the rigid end. The system is then back to the expansion after $t = \frac{3}{2}\pi$.

established surface concentration gradient that is higher at the rigid end. The capillary pressure, however, tends to drive the flow from the extensible end to the rigid end.

The system contracts between $t = \frac{1}{2}\pi$ and $t = \frac{3}{2}\pi$, and then expands between $t = \frac{3}{2}\pi$ and the end of the cycle. At $t = \frac{3}{2}\pi$ the wall contracts to its minimum length, but is instantaneously at rest again. Similar to $t = \frac{1}{2}\pi$, a counterclockwise vortex also appears at $t = \frac{3}{2}\pi$. In fact, the streamline patterns during contraction are just the reverse of those during expansion. This is because the $O(\Delta)$ solution is in the form given by

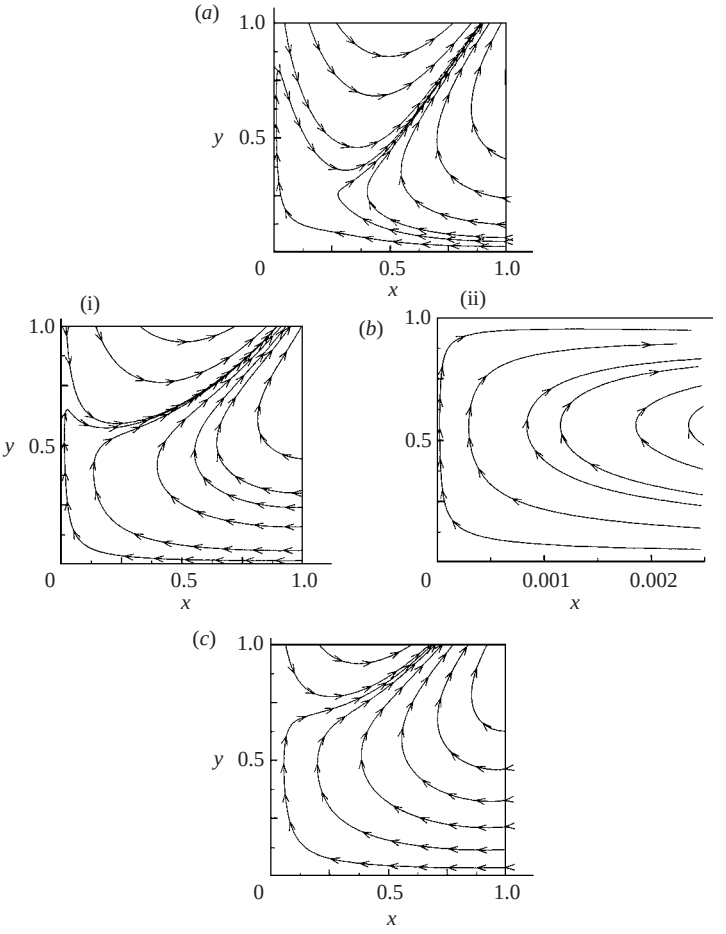

FIGURE 5. The $O(\Delta^2)$ cycle-averaged streamlines in the presence of an insoluble surfactant. (*a*) $M = 0.1$, (*b*) $M = 1.0$, (*c*) $M = 10.0$. $\hat{C}a = 1$, $Ps = 10$, $V_0 = 1$. The streamlines are calculated by (3.36). Note that the true horizontal scale (a_0) is much longer than the vertical one (*d*). The rigid end (the extensible end) is at $x = 0$ ($x = 1$). At first glance, the upper part of the fluid flows towards the extensible end while the lower portion of the fluid flows towards the rigid end. The higher M is the smaller the portion of the fluid that flows towards the rigid end. (*b*) (ii) is a zoom-in view of (*b*) (i) in order to compare with the corresponding inner solution in figure 13(*a*).

(3.29). The resulting cycle-averaged quantities are thus zero. Non-symmetry between expansion and contraction and non-zero cycle-averaged quantities appears at $O(\Delta^2)$.

The $O(\Delta)$ unsteady streamlines during a stretching cycle for a soluble surfactant are also shown in figure 4. The streamline patterns are qualitatively similar to those shown in figure 3 for an insoluble surfactant. However, as we shall see next, depending on the range of parameters, a soluble surfactant can significantly change the streamline patterns at $O(\Delta^2)$.

5.2. $O(\Delta^2)$ *cycle-averaged streamlines in the outer* (*core*) *region*

As mentioned above, steady streaming or non-zero cycle-averaged flow fields occur at $O(\Delta^2)$. Streamlines presented here are drawn in the Eulerian frame. Figure 5 shows $O(\Delta^2)$ cycle-averaged streamlines with different Marangoni numbers, M, for

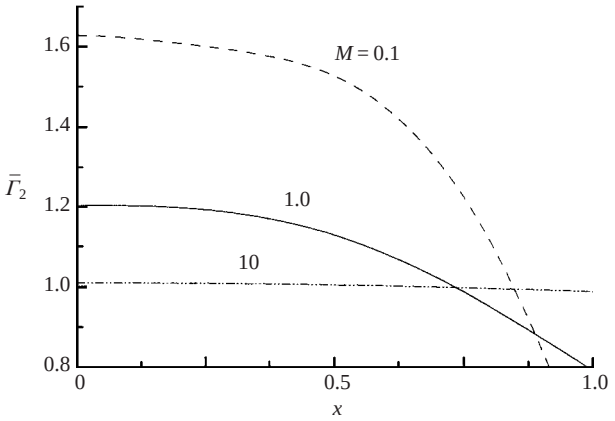

FIGURE 6. The $O(\Delta^2)$ cycle-averaged surface concentration $\overline{\Gamma}_2$ versus x corresponding to figure 5. The rigid end (the extensible end) is at $x = 0$ ($x = 1$). $\overline{\Gamma}_2$ is higher near the rigid end and decreases as it approaches the extensible end. The gradient of $\overline{\Gamma}_2$ diminishes as M increases.

an insoluble surfactant. At first glance, the upper portion of the fluid flows towards the extensible end while the lower portion flows towards the rigid end. This suggests that the system is favourable to exhalation, since flow resistance is lower as the liquid thickness becomes gradually thicker during the contraction. Even though the cycle-averaged wall velocity is zero, it can generate non-zero cycle-averaged capillary and Marangoni flows. The contraction motion tends to sweep the surfactant from the extensible end to the rigid end, and thus the associated Marangoni force along the interface drives the flow to the extensible end. However, this Marangoni flow competes against the capillary-driven flow. As shown in figure 5, the higher the value of M, the smaller the portion of fluid that flows towards the extensible end. Figure 5(b)(ii) is a zoom-in view of figure 5(b)(i) for the core lubrication flow near the rigid end. Later, we will compare figure 5(b)(ii) with that of the inner solution. For even higher $M(> 10)$, the streamline patterns do not change significantly because, as we shall see in figure 6, in this case, the surface concentration gradient almost vanishes and the interface becomes almost immobile.

To confirm the above observations in figure 5, figures 6 and 7 illustrate the cycle-averaged surface concentration $\overline{\Gamma}_2$ and the correction to the static liquid thickness $\overline{h}_2$, respectively. As shown in figure 6, $\overline{\Gamma}_2$ is higher near the rigid end and decreases as the extensible end is approached. For a small $M(= 0.1)$, the gradient of $\overline{\Gamma}_2$ is rather steep near the extensible end. Examining figure 5(a), the distinction between the forward and reversed flows seems to be nearly a straight line. This suggests that Marangoni flow, whose horizontal velocity is linear in y, is rather strong. Further increasing M reduces the level of $\overline{\Gamma}_2$. At large enough $M(> 10)$ the surface concentration is smaller because it is easier to generate the Marangoni force. In this case, the large Marangoni stress causes the interface to be almost tangentially immobile (but the normal interfacial velocity is non-zero). Since the interface is almost rigid for large enough M, the corresponding cycle-averaged streamlines do not further change. For the interface shape as shown in figure 7, the interface does not change significantly as M changes. This is because a strong capillary force serves as a restoring force when the interface is deformed. More importantly, the liquid thickness is thicker than the static ($\Delta = 0$) state and exhibits a convex shape. These results of both $\overline{\Gamma}_2$ and

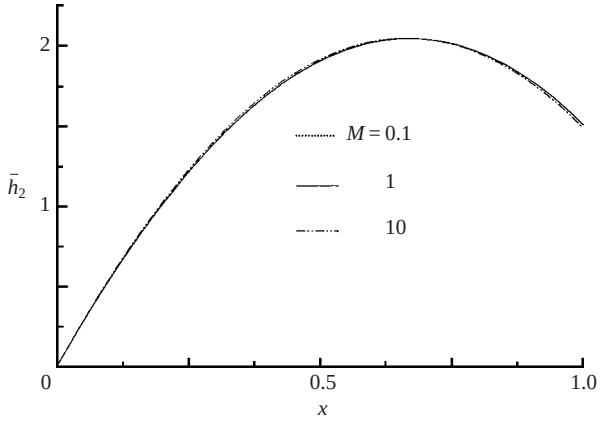

FIGURE 7. The $O(\Delta^2)$ cycle-averaged correction to the liquid thickness $\overline{h}_2$ versus x corresponding to figure 5. The rigid end (the extensible end) is at $x=0$ ($x=1$). The liquid thickness is greater than the static ($\Delta=0$) state.

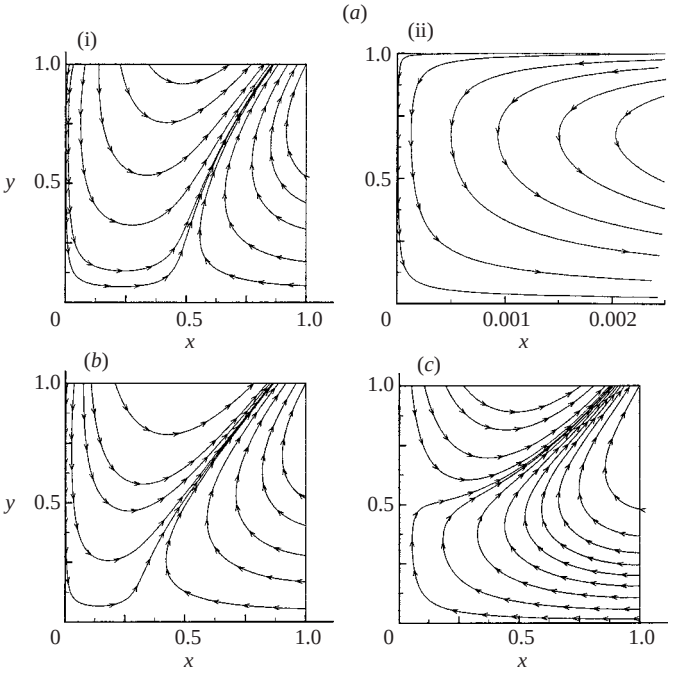

FIGURE 8. The $O(\Delta^2)$ cycle-averaged streamlines in the presence of a soluble surfactant. (*a*) $\beta=0.1$, (*b*) $\beta=1.0$, (*c*) $\beta=10.0$. $\hat{C}a=1$, $M=1$, $Ps=10$, $Pe_b=1$, $K=1$, $V_0=1$. The streamlines are calculated by (3.36). Note that the true horizontal scale (a_o) is much longer than the vertical one (d). The rigid end (the extensible end) is at $x=0$ ($x=1$). In comparison with insoluble cases as in figure 5, a greater portion of the fluid flows towards the extensible end, particularly for smaller β (higher solubility). Figure 8(*a*)(ii) is a zoom-in view of (*a*)(i) in order to compare with the corresponding inner solution in figure 13(*b*).

$\overline{h}_2$ profiles support the idea that contraction (expiration) motion is more favourable than expansion (inspiration).

We shall now turn our attention to cases involving a soluble surfactant. Figure 8 presents cycle-averaged streamlines of soluble cases with different β. Figure 8(*a*)(ii)

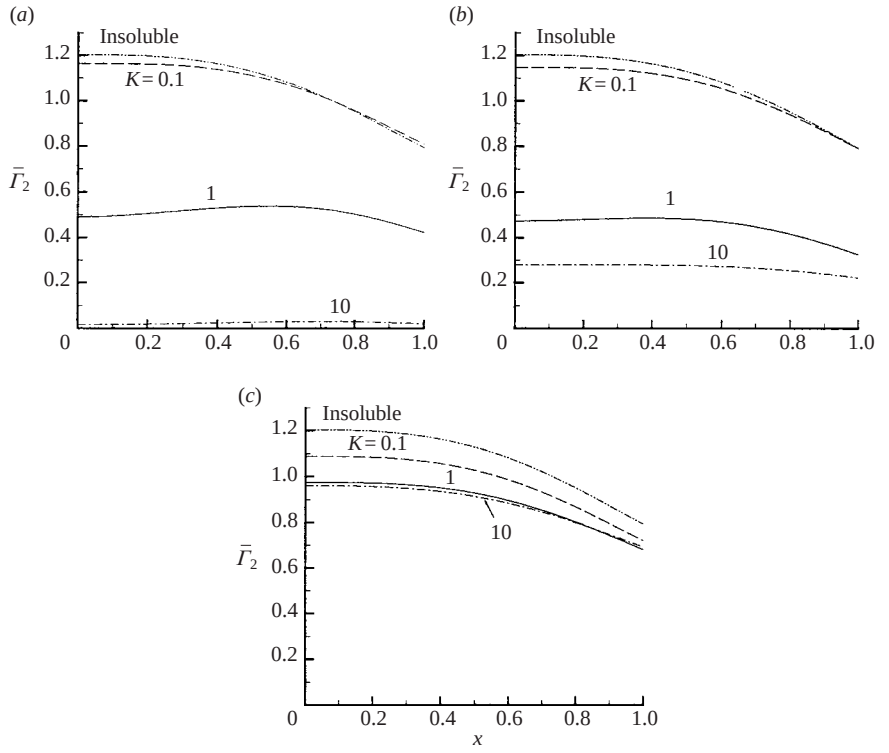

FIGURE 9. The $O(\Delta^2)$ cycle-averaged surface concentration $\overline{\Gamma}_2$ versus x with different K for (*a*) $\beta = 0.1$, (*b*) $\beta = 1.0$, (*c*) $\beta = 10.0$. $\hat{C}a = 1$, $M = 1$, $Ps = 10$, $Pe_b = 1$, $V_0 = 1$. The rigid end (the extensible end) is at $x = 0$ ($x = 1$). Lower β implies higher solubility of surfactant. Increasing K enhances the sorption kinetics and thus tends to diminish the gradient of $\overline{\Gamma}_2$.

is a zoom-in view of figure 8(*a*)(i) of the flow near the rigid end for comparison with the inner solution as discussed later. For high $\beta = 10$, the surfactant behaves like an insoluble surfactant and the resulting streamlines are similar to those for the insoluble case. As solubility increases by decreasing β, figures 8(*a*) and 8(*b*) show more portions of the fluid flow towards the extensible end. As we shall see below, this alteration of cycle-averaged stream patterns is related to the cycle-averaged surface concentration distribution.

Figure 9 shows $\overline{\Gamma}_2$ as a function of x for different combinations of β and K. Most trends are similar to those of the insoluble cases. As expected, large β or small K tends to approach the insoluble behaviour because the solubility or sorption flux becomes small. For β not large, as shown in figures 9(*a*) and 9(*b*), increasing K lowers the surface concentration and diminishes the surface concentration gradient since the system tends to reach equilibrium between the bulk and the surface concentration. However, for smaller β in figure 9(*a*), larger $K(\geqslant 1)$ seems to have a maximum surface concentration in the middle region. For $\beta = 0.1$ and $K = 1$ in figure 9(*a*), desorption is much faster than adsorption but its time scale is comparable to that of the stretching motion. Contraction enriches the surface concentration near the rigid end on the one hand; comparable desorption decreases the surface concentration on the other hand. This competition may lead to a local maximum or minimum of the surface concentration distribution. A similar competition between adsorption, desorption and the stretching motion can be found for $\beta = 1$ and $K = 1$. Its subsequent

surface concentration distribution is shown in figure 9(*b*). Recall that the resulting cycle-averaged streamlines for $(\beta, K) = (0.1, 1.0)$ and $(\beta, K) = (1.0, 1.0)$ are shown in figures 8(*a*) and 8(*b*), respectively. These non-trivial surface concentration distributions lead the fluid near the rigid end to flow towards the extensible end in contrast to the insoluble cases in which part of the fluid near the rigid end flows towards the extensible end. For larger β, as in figure 9(*c*), the surface concentration level is not effectively lowered by increasing K, because the solubility of the surfactant (i.e. diffusive flux from the bulk) is so low that sorption kinetics is not fast enough to reach equilibrium.

5.3. *Comparison with previous studies*

Podgorski and Gradon (Gradon & Podgorski 1989; Podgorski & Gradon 1990, 1993) investigated the mechanism of clearance flows or liquid pumping in an alveolus. Podgorski & Gradon (1991) and Espinosa & Kamm (1997) performed similar studies for the liquid lining of an airway. All studies of Podgorski and Gardon only considered insoluble surfactant. Espinosa & Kamm (1997) employed a more sophisticated sorption kinetics model accounting for the contribution from soluble surfactants. They, however, assumed a constant bulk concentration that lacks the variation of the bulk concentration caused by interfacial surfactant being desorbed into or absorbed out of the bulk. Our model considers solubility (via β) of surfactant that couples with the bulk concentration. When β is small (i.e. a high solubility), the surfactant transport is sorption-controlled from (2.35) and the bulk concentration is almost constant. It is equivalent to the assumption that Espinosa & Kamm (1997) used for the bulk concentration. As shown in figure 8, increasing β leads to different stream patterns in the lower part (say, $y < 0.5$) of the domain.

These previous studies focused on the role of the Marangoni force in determining clearance flows in a normal lung. Since surface tension forces are weak in a normal lung, their studies exclude capillarity as we shall justify later. All of their results suggest that the Marangoni force enhances clearance flows toward the more rigid end. Our study has accounted for capillarity since we can consider the high-tension regime due to surfactant deficiency. An additional difference from previous works is the use of boundary conditions at the alveolar outlet. Previous studies specified the surfactant concentration at the alveolar opening (or the more rigid end of an airway), and allowed net surfactant and fluid transport into or out of the system. In our analysis, we impose no flux boundary conditions at the alveolar opening for both surfactant and fluid.

To compare with previous studies that exclude the capillarity, we must demonstrate how the surface tension force modifies the cycle-averaged flow patterns. To do so, we shall fix the strength of the Marangoni force. Figure 10 show the effect of varying $\hat{Ca}$ with fixed $M/\hat{Ca} = 1$ on the cycle-averaged flow patterns in the presence of an insoluble surfactant. Notice that fixed $M/\hat{Ca} = -(\Gamma^*_\infty/\mu\omega a)(\partial\sigma^*/\partial\Gamma^*)_0$ means fixed strength of the Marangoni force while $\hat{Ca}$ varies. This is equivalent to changing the strength of surface tension. Also note that $\hat{Ca}$ is not restricted to $O(1)$ according to the discussion in § 2.2, we can extend its range for the large $\hat{Ca}$ (low-tension) regime. As shown in figure 10, a larger portion of the fluid tends to flow towards the rigid end as $\hat{Ca}$ increases. For the previous studies for modelling a normal lung, $\sigma^*_0 = 1 \sim 10$ dyn cm^{-1} gives $Ca = 10^{-4} \sim 10^{-5}$ or $\hat{Ca} = 10^4 \sim 10^5$ for $\varepsilon = 10^{-3}$ (layer thickness = 0.1 μm), thus the capillary term is negligible in their studies. Nevertheless, the flow pattern of figure 10(*c*) for $\hat{Ca} = 100$ sufficiently captures the flow tendency (i.e. the flow towards the alveolar opening) in the low-tension regime and qualitatively agrees with those

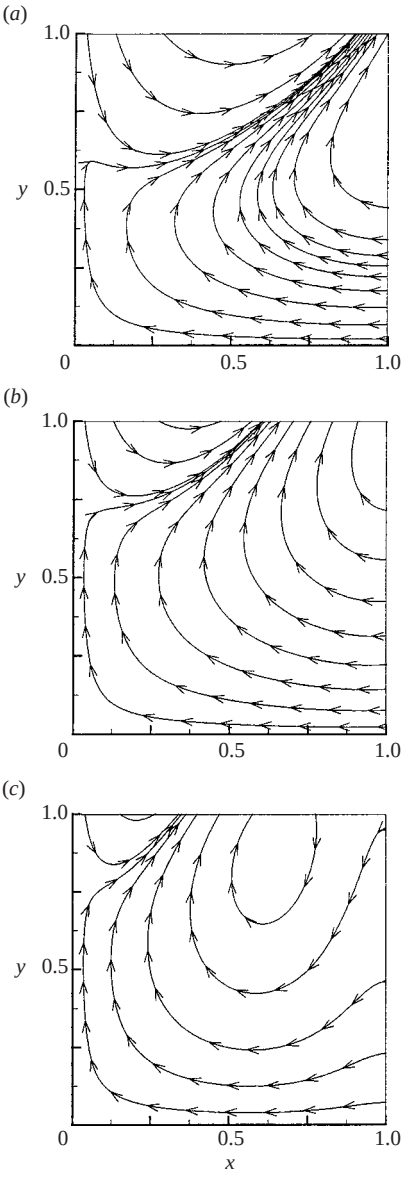

FIGURE 10. The $O(\Delta^2)$ cycle-averaged streamlines in the presence of an insoluble surfactant. (a) $\hat{C}a = 1$, (b) $\hat{C}a = 10$, (c) $\hat{C}a = 100$. $M/\hat{C}a = 1$, $Ps = 10$, $V_0 = 1$. The streamlines are calculated by (3.36). The true horizontal scale (a_0) is much longer than the vertical one (d). The rigid end (the extensible end) is at $x = 0$ ($x = 1$). Changing $\hat{C}a$ at fixed $M/\hat{C}a$ is equivalent to altering the surface tension with the fixed strength of the Marangoni force. Reducing surface tension promotes more flow towards the rigid end.

of previous investigations. Such similar flow features also suggest that the geometry effect of an alveolus may not be a major factor to change the flow qualitatively.

The above qualitative agreement also suggests that the qualitative features of such a flow system may not be too sensitive to detailed boundary conditions at the alveolar outlet. More importantly, the fact that the less upper portion of the fluid flows towards the extensible end for large $\hat{C}a$ suggests that the presence of the surface

tension force somehow diminishes the flow out of an alveolus owing to the Marangoni effect. Therefore, sufficiently strong surface tension could compromise the clearance process. This could have a critical implication to clinical applications such as PLV. For example, when the fluid thickness during PLV is 10 times thicker than normal, $\varepsilon = 10^{-2}$ is still within the validity of our model. In this case, $\hat{C}a = 10$ for $\sigma_0^* = 10$ dyn cm^{-1}, say owing to insufficient surfactant. If a given strength of the surfactant activity results in the situation as in figure 10(*b*), it then reduces the surface flow towards the alveolar opening, and thus discourages clearance processes.

5.4. *The Eulerian and Lagrangian drift velocities*

The cycle-averaged motion of fluid particles in the Lagrangian reference frame can be calculated from the Eulerian velocity field derived in § 3 for the core region. The Lagrangian velocity vector $\boldsymbol{V}$ is defined by

$$\boldsymbol{V} = \left(\frac{\partial \boldsymbol{X}}{\partial t}\right)_{\boldsymbol{X}_0}, \tag{5.1}$$

where the vector $\boldsymbol{X}(\boldsymbol{X}_0, t)$ is the fluid mapping or trajectory and $\boldsymbol{X}_0$ is the reference position. We expand the mapping in small Δ by

$$\boldsymbol{X} = \boldsymbol{X}_0 + \Delta \boldsymbol{X}_1(\boldsymbol{X}_0, t) + \Delta^2 \boldsymbol{X}_2(\boldsymbol{X}_0, t) + O(\Delta^3). \tag{5.2}$$

The corresponding expansion for (5.1) is related to the Eulerian velocity expansion $\boldsymbol{v} = \boldsymbol{v}_0(\boldsymbol{x}) + \Delta \boldsymbol{v}_1(\boldsymbol{x}, t) + \Delta^2 \boldsymbol{v}_2(\boldsymbol{x}, t) + O(\Delta^3)$, knowing that $\boldsymbol{v}_0 = 0$. At $\boldsymbol{x} = \boldsymbol{X}_0$, this yields

$$\boldsymbol{V}_1 \equiv \boldsymbol{X}_{1t} = \boldsymbol{v}_1, \tag{5.3a}$$

$$\boldsymbol{V}_2 \equiv \boldsymbol{X}_{2t} = \boldsymbol{v}_2 + \boldsymbol{X}_1 \cdot \nabla \boldsymbol{v}_1. \tag{5.3b}$$

$\boldsymbol{v}_1$ is obtained by integrating (5.3*a*) and is then substituted into (5.3*b*). We then take the cycle average of (5.3*b*), which yields the steady Lagrangian drift velocity $\overline{\boldsymbol{V}}_2$. Figure 11 shows the steady axial Eulerian drift velocities $\overline{u}_2$ across the liquid thickness at different x positions for both insoluble and soluble cases. They are qualitatively similar: the lower (upper) potion of the fluid flows towards the rigid end (extensible end). The flow strength for the soluble case seems to be a little weaker than that for the insoluble case.

The steady axial Lagrangian drift velocities $\overline{U}_{L2}$ are also shown in figure 12. They are rather different to the Eulerian results. The Lagrangian drift velocities for the upper part of the fluid are toward the rigid end, whereas those for the lower part are in the opposite direction. The Lagrangian drift velocities are about an order of magnitude smaller than the corresponding Eulerian ones.

5.5. *Cycle-averaged flow in the inner (rigid end) region*

We have imposed the pinned-end condition at the rigid end and also do not allow fluid and surfactants across the rigid endwall for describing the boundary conditions near the alveolar junction. The true boundary conditions near the junction may be complex. It is interesting to see how the boundary condition at the rigid end alters the flow feature. We have noticed that the vertical velocity (3.7*b*) of the outer solution does not satisfy the no-slip condition (2.28) at the rigid endwall ($x = 0$). This suggests that, if we replace the no-slip condition with a slip condition, but keep the rigid endwall impermeable, then the outer solution remains unchanged.

For other boundary conditions, we may choose a fixed contact angle but vary d (i.e. a moving contact line). In this case, surfactant may either accumulate or be

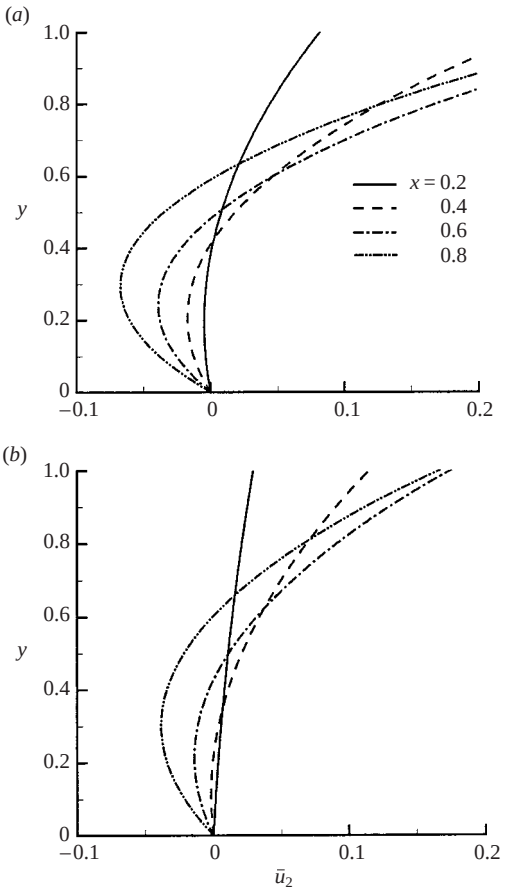

FIGURE 11. The $O(\Delta^2)$ steady Eulerian axial drift velocities: (*a*) insoluble case with $\hat{C}a = 1$, $M = 1$, $Ps = 10$, $V_0 = 1$, (*b*) soluble case with $\hat{C}a = 1$, $M = 1$, $Ps = 10$, $Pe_b = 1$, $K = 1$, $V_0 = 1$.

depleted near the moving contact point, depending on the slip velocity model. The resulting cycle-averaged surfactant distribution may behave differently and the corresponding steady streaming may be altered. If the surface concentration at the rigid end is fixed instead of setting its derivative to be zero, we expect that the resulting gradient of the surfactant concentration can generate a non-zero net flow that requires an additional flow source or sink to replace the fluid for remaining homeostasis (Zelig & Haber 2002). Such a case would be similar to the previous works (Gradon & Podgorski 1989; Podgorski & Gradon 1990; Espinosa & Kamm 1997).

We now discuss the inner flow region of the present model. The outer core solution breaks down near the rigid end. In this inner region, the interface remains flat because of a small capillary number ($\varepsilon Ca = \mu\omega d/\sigma_0^* \sim \varepsilon^4$). In addition, (4.9) suggests that Marangoni stresses also dominate the tangential stress along the interface for $M \sim O(1)$ and $Ca \sim \varepsilon^3$. Thus, the surface concentration is spatially uniform. For fast diffusion $\varepsilon^2 Pe_b \ll 1$, the bulk concentration is also spatially uniform. This leads the axial interfacial velocity to be proportional to the distance from the rigid endwall (see (4.33)). Because there is no cycle-averaged motion of the bottom wall, both non-zero cycle-averaged interfacial flow and the outer-region flow drive the flow in

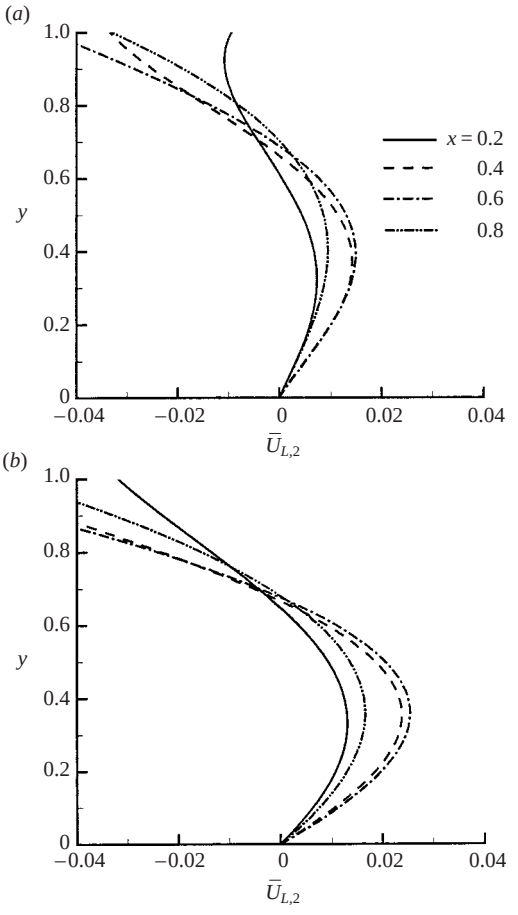

FIGURE 12. The $O(\Delta^2)$ steady Lagrangian axial drift velocities (a) and (b) corresponding to figures 11(a) and 11(b), respectively.

the inner region. Figure 13 shows typical cycle-averaged streamlines near the rigid end. As expected, the fluid coming from the upper (lower) portion of the domain turns around when it is against the rigid endwall, and then it flows out in the lower (upper) portion of the fluid. As shown in (4.40) and (4.41), the inner flow's direction is determined by the sign of $\overline{\Gamma}_{2xx}(x \to 0)$ or $(\overline{h}_{2xxxx} + \overline{h}_{2xx})(x \to 0)$ which depends on the system parameters. For an insoluble case of $M = 1$ as in figure 6, the cycle-averaged surface concentration has $\overline{\Gamma}_{2xx}(0) = -0.1044 < 0$. The resulting inner flow turns clockwise as in figure 13(a). To compare it with the outer steady streamlines near the rigid end, figure 5(b)(ii) is a zoom-in picture for regions near the rigid end of figure 5(b)(i). The horizontal scale of figure 5(b)(ii) is chosen the same as figure 12(a) for $\varepsilon = 0.001$, i.e. $x = \varepsilon X = 0.001X$. As a result, the turning direction of the flow near the rigid end is consistent with figure 13(a). Because the outer solutions satisfy the impermeable condition near the rigid end, the rigid endwall is thus a streamline. However, for a soluble case as in figure 9(a) for $\beta = 0.1$ and $K = 1$, the surface concentration profile can have $\overline{\Gamma}_{2xx}(0) = 0.9685 > 0$. Figure 13($b$) shows that the inner flow turns counterclockwise. It is also consistent with the corresponding steady outer streamlines of figure 8(a) that the fluid near the rigid end flows from the interface side and then turns towards the extensible end near the bottom wall.

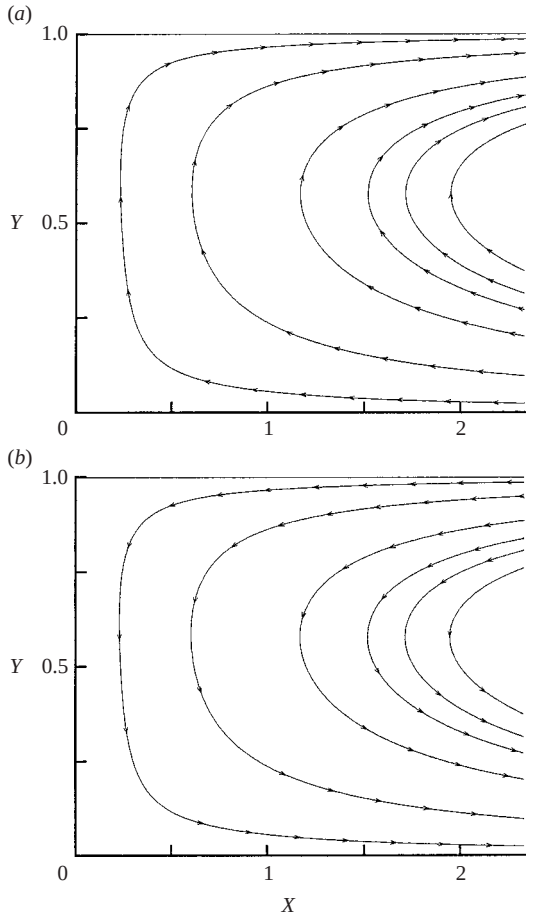

FIGURE 13. The $O(\Delta^2)$ steady inner streamlines. (a) Insoluble case with $\hat{C}a = 1$, $M = 1$, $Ps = 10$, $V_0 = 1$, the corresponding outer streamline is shown in figure 5(b)(ii). (b) Soluble case with $\hat{C}a = 1$, $M = 1$, $Ps = 10$, $Pe_b = 1$, $K = 1$, $\beta = 0.1$, $V_0 = 1$, the corresponding outer streamline is shown figure 8(a)(ii). The inner streamlines are calculated by (4.43). Note that the direction of the returning flow against the rigid wall is determined by the sign of $\overline{\Gamma}_{2xx}(x \to 0)$. By examining figure 9($a$), $\overline{\Gamma}_{2xx}(x \to 0) < 0$ for the insoluble case in figure 13(a), but $\overline{\Gamma}_{2xx}(x \to 0) > 0$ for the soluble case in figure 13(b).

5.6. *The effect of liquid volume*

The results we have discussed so far are based on uniform film thickness for $\Delta = 0$. This means that the flow (particularly near the rigid end) may be sensitive to the condition at the rigid end whose height is the same as the unperturbed liquid thickness. The detailed boundary conditions at the rigid end are not known in the real system, but whatever conditions exist, they must have zero net flow for the adjacent alveolus that are away from the terminal bronchioles. As shown in § 5.3, despite different boundary conditions applied in the present and previous models, similar qualitative features imply that detailed boundary conditions at the rigid end may not significantly change the flow features.

Since the rigid-end condition we imposed for the condition near the alveolar junction is somewhat speculative, one aim of this section is to examine the circumstances

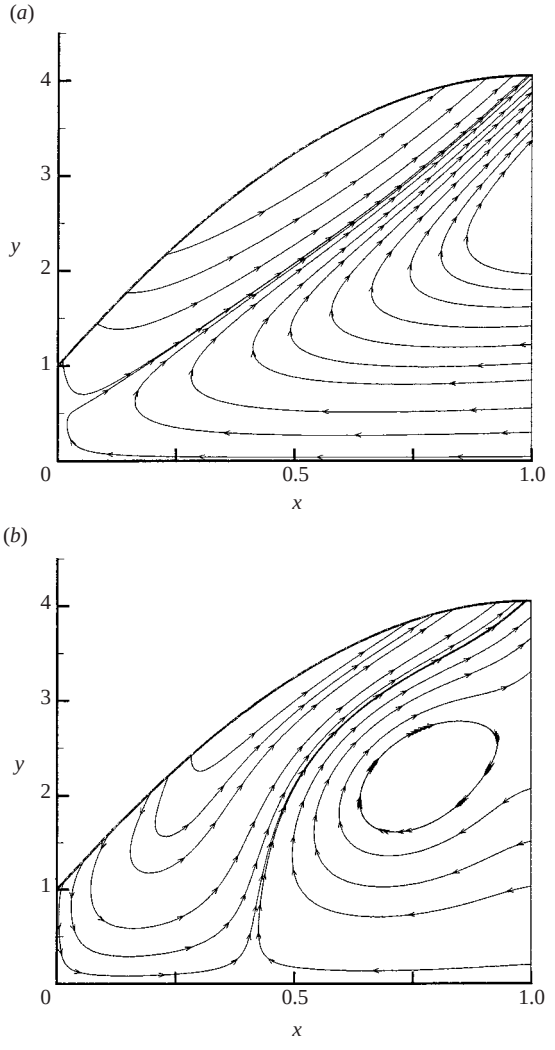

FIGURE 14. The $O(\Delta^2)$ cycle-averaged streamlines. (*a*) Insoluble case with $\hat{C}a = 1$, $M = 1$, $Ps = 10$, $V_0 = 3$. (*b*) Soluble case with $\hat{C}a = 1$, $M = 1$, $Ps = 10$, $Pe_b = 1$, $K = 1$, $\beta = 0.1$, $V_0 = 3$.

to see if this rigid-end condition is more important or not. As suggested in figure 1(*b*) for alveolar geometry, the liquid thickness near the alveolar junction seems to be thinner than in the remaining part of the layer owing to the presence of sharp edges. We speculate that the flow contribution near the alveolar junction could be less significant if the rest of the fluid layer is relatively thick. The impact of the rigid-end condition on the flow could be therefore minimized. To examine this, we increase V_0 from 1 (uniform layer thickness) to 3. Figures 14(*a*) and 14(*b*) show the cycle-averaged streamlines for insoluble and soluble surfactants, respectively. These stream patterns show similar trends in most parts of the domain compared to those of uniform thickness cases as in figures 5 and 8. However, a larger liquid volume leads to smaller regions of returning flows near the rigid end than in uniform thickness cases. The soluble surfactant case with $V_0 = 3$ exhibits a vortex near the extensible end while that with $V_0 = 1$ does not.

The fact that the flow features of a large liquid volume are similar to those of a smaller volume is not surprising because only the no-penetration condition at the rigid end is satisfied by the outer core flow that is dominant. In addition, as we examine the inner solution, the liquid thickness remains the same as the height of the rigid end. Because the liquid volume does not directly enter into the inner problem, the inner solution is passively determined by the information of the outer core flow that is affected by the liquid volume. Also, because a large liquid volume further enhances the contribution from the core flow, the impact of the presence of the rigid end is further diminished. We also notice that the no-cross-flow condition at the rigid end, with fixed film height, allows us to consider our solution as satisfying a spatially periodic configuration such as a cluster of alveoli.

6. Conclusion

We have developed a two-dimensional model to study the effects of breathing motion on fluid flow in the alveolar liquid lining in the presence of insoluble or soluble surfactants. We assume that the alveolar wall's motion is prescribed by a uniform strain. For a small aspect ratio ε and strain amplitude Δ ($\Delta^2 \gg \varepsilon$), we use scaling analysis and asymptotic theory to solve transport problems in both the outer (core) and inner (boundary layer) regions at leading order in ε with small-Δ expansions. The analysis is based on scalings of $Ca \sim \varepsilon^3$ and $M \sim O(1)$ for dilute ($O(\varepsilon^2)$) surfactant concentrations. The competition between the wall's stretching motion, the capillarity and the Marangoni effect is elucidated for various ranges of the parameters.

In the core region, we apply lubrication theory to derive a coupled set of evolution equations governing the liquid thickness, the surface concentration and the bulk concentration of surfactant. The results do not contribute to cycle-averaged quantities until $O(\Delta^2)$. The cycle-averaged streamline patterns show that the system is favourable to the expiration phase. This is suggested because the cycle-averaged liquid thickness is greater than in the non-stretching state and the surfactant concentration is lower near the extensible end. We qualitatively compare the present results with the previous studies that exclude capillary forces (Espinosa & Kamm 1997; Gradon & Podgorski 1989; Podgorski & Gradon 1990, 1993). The capillarity tends to enhance the flow towards the extensible end and diminishes the clearance process.

For the inner (rigid end) region, we solve analytically for the cycle-averaged inner flow fields using matched asymptotic principles and Laplace transform techniques. With the present scalings, the interface remains flat. Both the surface and the bulk concentrations are spatially uniform owing to the strong Marangoni force and the fast bulk diffusion. The inner steady flow patterns turn around when they are against the rigid endwall. For certain ranges of β and K, the turning direction of a soluble surfactant case can be opposite to that of an insoluble case.

Applying larger liquid volume diminishes the influence of the detailed flow boundary conditions at the rigid end. Since the primary flow contribution comes from the core region that does not satisfy the no-slip boundary conditions at the rigid end, our current study can be extended to model flow in a cluster of alveoli.

For a signalling process that requires molecules to transport back and forth between communicating cells, the cyclic unsteady flow velocity could be critical in addition to the steady flow. Our analysis estimates a characteristic dimensional unsteady axial velocity $u^* \sim 10^{-3}\,\mathrm{cm\,s^{-1}}$. The Péclet number is $Pe = u^* a_0 / D_m \sim 10^{-5}/D_m$, where D_m ($\mathrm{cm^2\,s^{-1}}$) is the diffusivity of molecules. For molecules with $D_m \sim O(10^{-5}\,\mathrm{cm^2\,s^{-1}})$ or smaller, $Pe \sim O(1)$ or larger which suggests that detailed knowledge of the

convection patterns is important for understanding this potential route for signalling. For steady molecular transport processes the steady axial velocity is $\overline{u}^* \sim 10^{-5}\,\mathrm{cm\,s^{-1}}$, and the corresponding steady Péclet number is $\overline{Pe} = \overline{u}^* a_0/D_m \sim 10^{-7}/D_m$. For $D_m \leqslant O(10^{-7}\,\mathrm{cm^2\,s^{-1}})$, such as the pulmonary surfactant DPPC, proteins, delivered surfactants, drugs and genetic material whose D_m is from 10^{-7} to $10^{-8}\,\mathrm{cm^2\,s^{-1}}$, this suggests that $\overline{Pe} \geqslant O(1)$, implying that convection governs the transport of such molecules.

This work was supported by NIH Grants HL41126 and HL64373.

REFERENCES

Bastacky, J., Lee, C. Y. C., & Goerke, J. *et al.* 1995 Alveolar lining layer is thin and continuous: low-temperature scanning electron microscopy of rat lung. *J. Appl. Physiol.* **79**, 1615–1628.

Benthem, J. P. 1963 A Laplace transform method for the solution of semi-infinite and finite strip problems in stress analysis. *Q. J. Mech. Appl. Maths* **16**, 413–429.

Borgas, M. S. & Grotberg, J. B. 1988 Monolayer flow on a thin film. *J. Fluid Mech.* **193**, 151–170.

Bull, J. L., Nelson, L. K., Walsh, J. T., Glucksberg, M. R., Schurch, S. & Grotberg, J. B. 1999 Surfactant-spreading and surface-compression disturbance on a thin viscous film. *J. Biomech. Engng* **121**, 89–98.

Corbet, A., Bucciarelli, R., Goldman, S., Mammel, M., Wold, D. & Long, W. 1991 Decreased mortality rate among small premature infants treated at birth with a single dose of synthetic surfactant: a multicenter controlled trial. *J. Pediat.* **118**, 277–284.

Cormack, D. E., Leal, L. G. & Imberger, J. 1974 Natural convection in a shallow cavity with differentially heated end walls. *J. Fluid Mech.* **65**, 209–229.

Crapo, J. D., Barry, B. E., Gehr, P., Bachofen, M. & Weibel, E. R. 1982 Cell number and cell characteristics of the normal human lung. *Am. Rev. Respir. Dis.* **126**, 332–337.

Davis, J. M., Russ, G. A., Metlay, L., Dickerson, B. & Greenspan, B. S. 1992 Short-term distribution kinetics of intratracheally administered exogenous lung surfactant. *Pediat. Res.* **31**, 445–450.

Edwards, D. A., Hanes, J., Caponetti, G. *et al.* 1997 Large porous particles for pulmonary drug delivery. *Science* **276**, 1868–1871.

Espinosa, F. F. & Kamm, R. D. 1997 Thin layer flows due to surface tension gradients over a membrane undergoing non-uniform, periodic strain. *Ann. Biomed. Engng* **25**, 913–925.

Espinosa, F. F., Shapiro, A. H., Fredberg, J. J. & Kamm, R. D. 1993 Spreading of exogenous surfactant in an airway. *J. Appl. Physiol.* **75**, 2028–2039.

Flotte, T. R. 1993 Prospects for virus-based gene therapy for cystic fibrosis. *J. Bioenerget. Biomembranes* **25**, 37–42.

Fox, W. W., Weis, C. M., Cox, C., Farina, C., Drott, H., Wolfson, M. R. & Shaffer, T. H. 1997 Pulmonary administration of gentamicin during liquid ventilation in a newborn lamb lung injury model. *Pediatrics* **100**, E5.

Gaver, D. P. & Grotberg, J. B. 1990 The dynamics of a localized surfactant on a thin film. *J. Fluid Mech.* **213**, 127–148.

Gradon, L. & Podgorski, A. 1989 Hydrodynamical model of pulmonary clearance. *Chem. Engng Sci.* **44**, 741–749.

Grotberg, J. B., Halpern, D. & Jensen, O. E. 1995 Interaction of exogenous and endogenous surfactant: spreading-rate effects. *J. Appl. Physiol.* **78**, 750–756.

Halpern, D. & Grotberg, J. B. 1992 Dynamics and transport of a localized soluble surfactant on a thin film. *J. Fluid Mech.* **237**, 1–11.

Halpern, D., Jensen, O. E. & Grotberg, J. B. 1998 A theoretical study of surfactant and liquid delivery into the lung. *J. Appl. Physiol.* **85**, 333–352.

Hirschl, R. B., Tooley, R., Parent, A. C., Johnson, K. & Bartlett, R. H. 1995 Improvement of gas exchange, pulmonary function, and lung injury with partial liquid ventilation. A study model in a setting of severe respiratory failure. *Chest* **108**, 500–508.

Jensen, O. E. & Grotberg, J. B. 1992 Insoluble surfactant spreading on a thin viscous film: shock evolution and film rupture. *J. Fluid Mech.* **240**, 259–288.

Jensen, O. E. & Grotberg, J. B. 1993 The spreading of heat or soluble surfactant along a thin liquid film. *Phys. Fluids* A **5**, 58–68.

Jobe, A. H. 1993 Pulmonary surfactant therapy. *New Engl. J. Med.* **328**, 861–868.

Joseph, D. D. 1977 The convergence of biorthogonal series for biharmonic and Stokes flow edge problems. Part I. *SIAM J. Appl. Maths* **33**, 337–347.

Joseph, D. D. & Sturges, L. 1978 The convergence of biorthogonal series for biharmonic and Stokes flow edge problems. Part II. *SIAM J. Appl. Maths* **34**, 7–26.

Krueger, M. A. & Gaver, D. P. 2000 A theoretical model of pulmonary surfactant multilayer collapse under oscillating area conditions. *J. Colloid. Interface Sci.* **229**, 353–364.

Lewis, J. F., Ikegami, M. & Jobe, A. H. 1992 Metabolism of exogenously administered surfactant in the acutely injured lungs of adult rabbits. *Am. Rev. Resp. Dis.* **145**, 19–23.

Lisby, D. A., Ballard, P. L., Fox, W. W., Wolfson, M. R., Shaffer, T. H. & Gonzales, L. W. 1997 Enhanced distribution of adenovirus-mediated gene transfer to lung parenchyma by perfluorochemical liquid. *Human Gene Therapy* **8**, 919–928.

Mates, E. A., Jackson, J. C., Hildebrandt, J., Truog, W. E., Standaert, T. A. & Hlastala, M. P. 1994 Respiratory gas exchange and inert gas retention during partial liquid ventilation. *Adv. Expl Med. Biol.* **361**, 427–435.

Meisner, D., Pringle, J. & Mezei, M. 1989 Liposomal pulmonary drug delivery. I. In vivo disposition of atropine base in solution and liposomal form following endotracheal instillation to the rabbit lung. *J. Microencapsul.* **6**, 379–387.

Podgorski, A. & Gradon, L. 1990 Dynamics of pulmonary surfactant system and its role in alveolar cleansing. *Ann. Occup. Hyg.* **34**, 137–147.

Podgorski, A. & Gradon, L. 1991 Function of the pulmonary surfactant in the clearance of respiratory bronchioles: a mathematical model. *Chem. Engng Commun.* **110**, 143–162.

Podgorski, A. & Gradon, L. 1993 An improved mathematical model of hydrodynamic self-cleansing of pulmonary alveoli. *Ann. Occup. Hyg.* **37**, 347–365.

Raczka, E., Kukowska-Latallo, J. F., Rymaszewski, M., Chen, C. & Baker, J. R. 1998 The effect of synthetic surfactant Exosurf on gene transfer in mouse lung in vivo. *Gene Therapy* **5**, 1333–1339.

Schurch, S., Bachofen, H., Goerke, J. & Possmayer, F. 1989 A captive bubble method reproduces the *in situ* behavior of lung surfactant monolayers. *J. Appl. Physiol.* **67**, 2389–2396.

Sen, A. K. & Davis, S. H. 1982 Steady thermocapillary flows in two-dimensional slots. *J. Fluid Mech.* **121**, 163–186.

Shaffer, T. H. & Wolfson, M. R. 1996 Liquid ventilation: an alternative ventilation strategy for management of neonatal respiratory distress. *Eur. J. Pediat.* **155** Suppl. 2, S30-4.

Stone, H. A. 1990 A simple derivation of the time-dependent convective–diffusion equations for surfactant transport along a deforming interface. *Phys. Fluids* A **2**, 111–112.

Tarczy-Hornoch, P., Hildebrandt, J., Standaert, T. A. & Jackson, J. C. 1998 Surfactant replacement increases compliance in premature lamb lungs during partial liquid ventilation *in situ*. *J. Appl. Physiol.* **84**, 1316–1322.

Waldrep, J. C., Gilbert, B. E., Knight, C. M., Black, M. B., Scherer, P. W., Knight, V. & Eschenbacher, W. 1997 Pulmonary delivery of beclomethasone liposome aerosol in volunteers – tolerance and safety. *Chest* **111**, 316–323.

Wolfson, M. R., Greenspan, J. S. & Shaffer, T. H. 1996 Pulmonary administration of vasoactive substances by perfluorochemical ventilation. *Pediatrics* **97**, 449–455.

Wright, J. R. & Clements, J. A. 1987 Metabolism and turnover of lung surfactant. *Am. Rev. Resp. Dis.* **136**, 426–444.

Yu, J. & Chien, Y. W. 1997 Pulmonary drug delivery: physiologic and mechanistic aspects. *Crit. Rev. Therapeut. Drug Carrier Syst.* **14**, 395–453.

Zelig, D. & Haber, S. 2002 Hydrodynamic cleansing of pulmonary alveoli. *SIAM J. Appl. Maths* **63**, 195–221.

Zelter, M., Escudier, B. J., Hoeffel, J. M. & Murray, J. F. 1990 Effects of aerosolized artificial surfactant on repeated oleic acid injury in sheep. *Am. Rev. Resp. Dis.* **141**, 1014–1019.